Quantitative WDS compositional mapping using the electron microprobe

JOHN J. DONOVAN[1],*, JULIEN M. ALLAZ[2],†, ANETTE VON DER HANDT[3], GARETH G.E. SEWARD[4], OWEN NEILL[5], KARSTEN GOEMANN[6], JULIE CHOUINARD[1], AND PAUL K. CARPENTER[7]

[1]CAMCOR, University of Oregon, Eugene, Oregon, 97403, U.S.A.
[2]Institute of Geochemistry and Petrology, ETH Zürich, 8092 Zürich, Switzerland
[3]Department of Earth Sciences, University of Minnesota, Minneapolis, Minnesota 55455, U.S.A.
[4]Department of Earth Science, University of California Santa Barbara, Santa Barbara, California 93101, U.S.A.
[5]Department of Earth and Environmental Sciences, University of Michigan, Ann Arbor, Michigan 48013, U.S.A.
[6]Central Science Laboratory, University of Tasmania, Hobart, Tasmania 7001, Australia
[7]Department of Earth and Planetary Sciences, Washington University in St. Louis, One Brookings Drive, St. Louis, Missouri 63130, U.S.A.

ABSTRACT

While much progress has been made in electron-probe microanalysis (EPMA) to improve the accuracy of point analysis, the same level of attention has not always been applied to the quantification of wavelength-dispersive spectrometry (WDS) X-ray intensity maps at the individual pixel level. We demonstrate that the same level of rigor applied in traditional point analysis can also be applied to the quantification of pixels in X-ray intensity maps, along with additional acquisition and quantitative processing procedures to further improve accuracy, precision, and mapping throughput. Accordingly, X-ray map quantification should include pixel-level corrections for WDS detector deadtime, corrections for changes in beam current (beam drift), changes in standard intensities (standard drift), high-accuracy removal of background intensities, quantitative matrix corrections, quantitative correction of spectral interferences, and, if required, time-dependent corrections (for beam and/or contamination sensitive materials). The purpose of quantification at the pixel level is to eliminate misinterpretation of intensity artifacts, inherent in raw X-ray intensity signals, that distort the apparent abundance of an element. Major and minor element X-ray signals can contain significant artifacts due to absorption and fluorescence effects. Trace element X-ray signals can contain significant artifacts where phases with different average atomic numbers produce different X-ray continuum (bremsstrahlung) intensities, or where a spectral interference, even an apparently minor one, can produce a false-positive intensity signal. The methods we propose for rigorous pixel quantification require calibration of X-ray intensities on the instrument using standard reference materials, as we already do for point analysis that is then used to quantify multiple X-ray maps, and thus the relative time overhead associated with such pixel-by-pixel quantification is small. Moreover, the absolute time overhead associated with this method is usually less than that required for quantification using manual calibration curve methods while resulting in significantly better accuracy. Applications to geological, synthetic, or engineering materials are numerous as quantitative maps not only show compositional 2D variation of fine-grained or finely zoned structures but also provide very accurate quantitative analysis, with precision approaching that of a single point analysis, when multiple-pixel averaging in compositionally homogeneous domains is utilized.

Keywords: EPMA, WDS, quantitative analysis, X-ray mapping, quantitative mapping

INTRODUCTION

Quantification of WDS X-ray intensities by electron-probe micro-analysis (EPMA) has progressed over the last few decades with the development of better instrument hardware for stable operation and improved software for physics-based background, matrix, and spectral interference corrections (Armstrong 1988; Donovan et al. 1993; Donovan and Tingle 1996). However, these advances have generally been limited to so-called "point analysis," by which we mean quantitative characterization of elemental chemistry, typically at a nominal volume of a cubic micrometer, when the beam and stage are stationary with respect to each other. This quantitative point analysis now approaches and may be better than 2% relative accuracy for major and even minor elemental concentrations in many compositional matrices. Additionally, these improvements in both hardware and software, combined with measurements at high-beam currents and extended integration times, have demonstrated sensitivity at ppm levels for quantitative point analysis in selected materials (e.g., Donovan et al. 2011; Batanova et al. 2015).

In practice, quantitative EPMA point analysis can be performed in minutes for a suite of elements and includes both background and matrix corrections. Conversely, X-ray maps obtain spatial information by limiting the dwell-time per pixel to hundreds to thousands of milliseconds, which, depending on

* E-mail: donovan@uoregon.edu
† Orcid 0000-0003-3783-0502

the pixel resolution and sensitivity required, can take hours to days of map acquisition time. These shorter pixel intensity integration times result in a reduction in precision due to counting statistics, but in principle, they do not reduce accuracy when the pixel intensity values are corrected using the same methods that are already utilized for conventional point analysis.

Some investigators have proposed using calibration curves for quantification of raw intensity X-ray maps, and such alternative quantification methods will be discussed below. However, except for specialized circumstances [e.g., trace carbon in steel (Eichen et al. 1972); low-voltage analysis (Moy et al. 2019)], such methods are problematic for optimal accuracy, especially in multiphase materials often encountered by geologists and material scientists.

It should be noted that the evaluation of raw X-ray intensity maps may be no better than comparing raw intensities from point measurements if the map interpretation depends on quantitative comparisons, as is usually the case. Analysts do not generally compare raw X-ray count rates when interpreting their point analyses, as these count rates include the bremsstrahlung ("background" or continuum X-ray signal) and are also subject to non-systematic variations due to matrix effects; likewise, count rates obtained during X-ray mapping are subject to these same effects, and therefore evaluation of raw intensity X-ray maps are subject to the same pitfalls (i.e., the same X-ray intensity can represent widely different concentrations from pixel to pixel depending on the composition of the specific pixel under examination). Science depends on accurate numerical quantification, and X-ray mapping should be no exception. This paper describes a quantification protocol for the treatment of WDS element X-ray maps obtained on the electron microprobe to yield the most accurate and precise results, just as we already do for our point analyses.

ACQUISITION OF X-RAY MAPS FOR QUANTIFICATION USING THE ELECTRON MICROPROBE

X-ray element mapping can be performed either using a wavelength-dispersive spectrometer (WDS) or a silicon-drift energy-dispersive spectrometer (EDS) with pros and cons for each detector. Modern silicon-drift EDS systems exhibit high throughput of X-ray intensities and can be important for element mapping of major elements. The main advantage of EDS is the simultaneous measurement of a wide range of X-ray energies during acquisition in a relatively short amount of time, i.e., a few seconds per point, although artifacts in EDS spectra (see below) can become problematic at typical high-beam currents necessary for efficient mapping. Unfortunately, when scanning over large areas and collecting X-rays as pixels, the counting statistics on a given pixel at a given energy channel are comparatively poor, and therefore the peak-to-background (P/B) ratios remain low. Moreover, EDS systems often exhibit high dead times at the elevated beam current values typically used for element mapping of minor and trace elements (>100–200 nA). At such high-beam currents, these tradeoffs result in utilizing either a shorter pulse processing time constant at the cost of poorer spectral resolution, which is not ideal for quantification or a longer pulse processing time constant by utilizing a reduced EDS-aperture size, which reduces sensitivity and introduces spectral artifacts. Furthermore, the development of pileup peaks and Si-escape peaks (Newbury

1995) complicates the quantitative analysis and interference correction of EDS spectra, although new EDS algorithms may offer better corrections for these artifacts (Newbury and Ritchie 2019).

Measurement by WDS has the superior advantages of higher P/B and X-ray counting rates as the X-ray wavelength of interest is selected by Bragg diffraction, and the counting electronics process only these selected pulses and automatically rejects most high-order X-ray line reflections when differential pulse height analysis (PHA) parameters are properly adjusted. These improved WDS P/B statistics and higher counting rates result in better analytical sensitivity, and they allow WDS to be used not only for major but also for minor and trace element measurement. WDS is also the preferred choice for routine analysis and element mapping of a wide range of phases and excels in the measurement of elements at trace element concentration and/or having low-energy X-rays (Goldstein et al. 1992). In this paper, we will limit ourselves to a discussion of quantitative analysis of WDS X-ray maps acquired with EPMA instruments.

Element mapping by WDS on the electron microprobe is usually performed by using a fixed electron beam ("spot" mode) in combination with specimen stage scanning motion, an approach referred to as "stage mapping." This fixed beam is used to avoid lateral defocusing of the spectrometer when scanning sample areas larger than the WDS Bragg focus dimension. During stage mapping, the image pixel dimension is defined by the stage motor step size, and the electron beam diameter is usually set equal to or slightly less than this pixel dimension. On JEOL microprobes, the stage sample holder is then scanned in y-axis strips with incremental movement of the x-axis starting on the top-right corner, and on Cameca microprobes the stage is scanned in x-axis strips with incremental movement of the y-axis starting on the top-left corner. These differences have implications for how the calculations for beam drift and standard intensity drift corrections are applied to the pixel acquisition order. It should also be noted that when stage maps are acquired over large sample areas or for long durations, both the flatness of the sample and the stability of the instrument are of paramount importance for X-ray map quantification. Any changes in the sample Z-axis focus or instrument stability can result in significant X-ray measurement errors due to changes in Bragg defocus and column and/or spectrometer alignment.

For higher spatial resolution, a beam scanning method with sub-micrometer pixel size is preferred to minimize stage reproducibility errors after each pixel strip and between multiple passes over the same area. This beam mapping method can only be performed on small areas, where Bragg defocusing effects are negligible (<20–40 μm lateral map dimensions, dependent on the WDS Rowland circle and the specific Bragg crystal). In either case, each pixel records the total X-ray count on each WDS channel, with each spectrometer tuned to an X-ray characteristic peak position of an element of interest. For multiphase samples with numerous major and minor elements to map, it is typically necessary to perform this acquisition using 1 to 3 or more passes over the same sample area; one pass for each set of WDS elements to be measured. For instance, on a 5-spectrometer microprobe, it is necessary to do two passes of 5 elements each to acquire up to 10 elements for a typical silicate analysis (usually Si, Al, Fe, Mn, Mg, Ca, Na, and K, and as required Ti, Cr, P, S,

Ni, or other trace or minor elements of interest).

For accurate map quantification, it is necessary to remove any intensities not pertaining to the characteristic X-ray to be quantified. First and foremost is the bremsstrahlung, which is commonly referred to as the X-ray continuum or X-ray background. The conventional background correction method for point analysis is to drive the WDS spectrometer to two off-peak positions, that is, to the sides of the characteristic X-ray peak position, to measure the X-ray intensity at a spectrometer position where only continuum X-rays satisfy Bragg's law. By extrapolating or interpolating such intensity values to the on-peak position, the continuum intensity under the peak can subsequently be determined. Such off-peak background measurements can also be acquired during quantitative X-ray mapping, but this requires the acquisition of not only an on-peak map, but also the additional acquisition of at least one (e.g., Cameca PeakSight software, https://www.cameca.com/), and ideally two background maps (Probe Software Probe Image software, https://probesoftware.com/), particularly for emission lines where the continuum spectrum is highly sloped or curved (e.g., at low-spectrometer limits; Jercinovic et al. 2012). If two background X-ray maps are acquired, an interpolation of the intensities is made at each pixel using linear, polynomial, exponential, or slope regression methods to obtain the background intensity to subtract from the on-peak X-ray map pixel intensity.

However, considerable acquisition time can be saved if no background X-ray maps are actually acquired, but instead the background intensity is constrained by a standards-based background calibration curve such as the mean atomic number (MAN) background correction method (Kramers 1923; Merlet and Bodinier 1990; Donovan and Tingle 1996). The use of the MAN background corrections does not require the acquisition of off-peak X-ray maps at all, thus resulting in not only significant savings in mapping acquisition time but also improved sensitivity due to the statistics of the MAN background correction method (Donovan et al. 2016). This approach is recommended and discussed further below.

CALIBRATION CURVE AND OTHER METHODS FOR X-RAY MAP QUANTIFICATION

Tinkham and Ghent (2005) have proposed X-ray map pixel quantification using Bence-Albee (hyperbolic) calibration curve methods, combined with a single standard MAN background correction, which they claim can produce quantitative X-ray maps, except in cases of high absorption or fluorescence (Donovan et al. 2019), or when mapping trace elements in multiphase materials with different average atomic numbers (see below for more details). However, since we already have more accurate analytical physics and background removal techniques available from point analysis methods, it is reasonable to apply our full knowledge of electron-microprobe physics to the analytical situation at hand, whether that application is point analysis or X-ray mapping.

Alternatively, some investigators (e.g., Lanari et al. 2014; Ortolano et al. 2018) have proposed quantifying raw X-ray maps by means of calibration curve methods. These methods attempt to relate the raw X-ray intensities in maps to concentrations determined from at least two or more single-point analyses that are considered representative of the range of compositions of

the different phases within the map area. From this, one can interpolate concentrations for a given arbitrary X-ray intensity. Although in principle this method appears to provide some usefulness for quantification of X-ray maps of a single phase, the nature of electron and X-ray physics informs us that when applied to situations with multiple phases, each with diverse matrix physics, these assumptions of compositional linearity are unfounded (Barkman et al. 2013; Donovan et al. 2019). Even worse are these assumptions, applied to trace minor and element analysis, when multiple phases with different average atomic numbers are present, as each zero concentration, i.e., the bremsstrahlung intensity at the peak position of interest, is represented by a different X-ray intensity. The calibration curve method is also unable to accurately correct for spectral peak interferences in different phases.

In systems with multiple phases, the same X-ray intensity in different phases can represent quite different elemental concentrations due to absorption and/or fluorescence effects. Similarly, the X-ray intensity corresponding to a zero concentration of an element depends wholly on the X-ray continuum absorption and on the average atomic number of the phase, which can vary significantly from one phase to another and sometimes even within one single phase exhibiting substantial compositional zonation. For example, $SiK\alpha$ intensity data obtained in multiple silicate reference materials plotted against the Si concentration do not lie on a linear line trend, and even an exponential calibration curve cannot be properly fitted (Fig. 1).
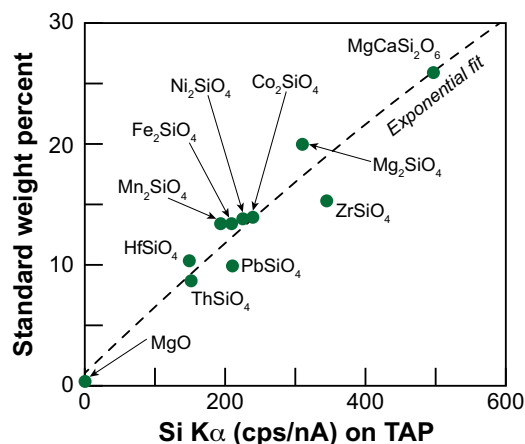

FIGURE 1. Example of an exponential calibration curve of Si concentrations as a function of X-ray intensities, for several standards each containing Si. Each green dot represents the average intensity for each standard. Errors on each standard measurement are smaller than the actual dot size (~0.5% relative for $SiK\alpha$ intensity).

TABLE 1. Differences in Si concentrations from standard reference published values, where the concentrations are derived from an exponential fit calibration-curve method to the raw Xray intensities, for synthetic zircon ($ZrSiO_4$) and synthetic forsterite (Mg_2SiO_4)

$SiK\alpha$, TAP, 20 keV, 30 nA	$ZrSiO_4$	Mg_2SiO_4
Published concentration of standard	15.32 wt%	19.96 wt%
Concentration from calibration curve (Fig. 1)	19.09 wt%	17.38 wt%
Relative error %	24.6%	−12.9%

Due to differences in the matrix correction physics for each of the phases plotted, there is insufficient linearity to robustly correlate intensity to concentration when more than a single phase is present or when a strong compositional zonation is observed and is not fully covered by the single-point analysis obtained in the phase of interest. It is, in fact, precisely for this reason that such calibration curves are very limited in application for EPMA point analysis quantification, with rare exceptions such as trace carbon in steel, where several reference materials of similar range in composition are considered (Robaut et al. 2006). These non-linearities are even more obvious when examining the numerical results from a generic multi-standard calibration curve, as seen in Table 1 for the analysis of several different standard materials. Clearly, we should expect better accuracy than this for our X-ray map quantification efforts.

A NEW METHOD FOR RIGOROUS QUANTIFICATION OF X-RAY MAPS

The method for quantitative X-ray mapping presented in this paper largely replicates the quantitative methods already developed for point analysis. The main difference is that the full set of correction algorithms are applied to intensities measured at each individual pixel in the X-ray map, rather than just a single discrete point. This process, summarized in Figure 2 and detailed in the following discussion, begins with the extraction of the array of raw counts obtained for all elements on each pixel, one pixel at a time. The counts received are corrected for dead time, and then normalized to the counting time and beam current to yield X-ray intensities in counts per second per nanoamp (cps/nA). These resulting intensities are then corrected for dead time, beam drift, standard intensity drift, background, and time-dependent intensity (TDI) corrections when necessary, e.g., for beam sensitive samples and for contamination issues such as trace carbon measurements. This whole correction procedure is then run iteratively through a full matrix correction, either ZAF or $\Phi(\rho z)$ methods, as required by the analyst, along with any quantitative spectral interference corrections specified by the user. Of course, the exact same normalization and correction procedures are also applied to the standard intensities from point measurements, which will be utilized not only in the construction of the intensity k-ratio prior to the matrix correction procedures but also in the calculation of the MAN (absorption corrected) background calibration curve for each analyzed element, and in the peak interference correction (if necessary) for the primary standards.

Dead time corrections and intensity normalization

The first step in the quantification of X-ray maps is to apply a dead time correction using a single factorial (Eq. 1a). However, when utilizing high beam currents to improve sensitivity, the count rate can exceed 50 000 counts per second, and a high-precision expression that extends the factorial to another term is usually preferred (Eq. 1b).

$$i_{dt} = \frac{i_{cps}}{1 - i_{cps} * \tau} \tag{1a}$$

$$i_{dt} = \frac{i_{cps}}{1 - \left(i_{cps} * \tau + i_{cps}^2 * \frac{\tau^2}{2}\right)} \tag{1b}$$
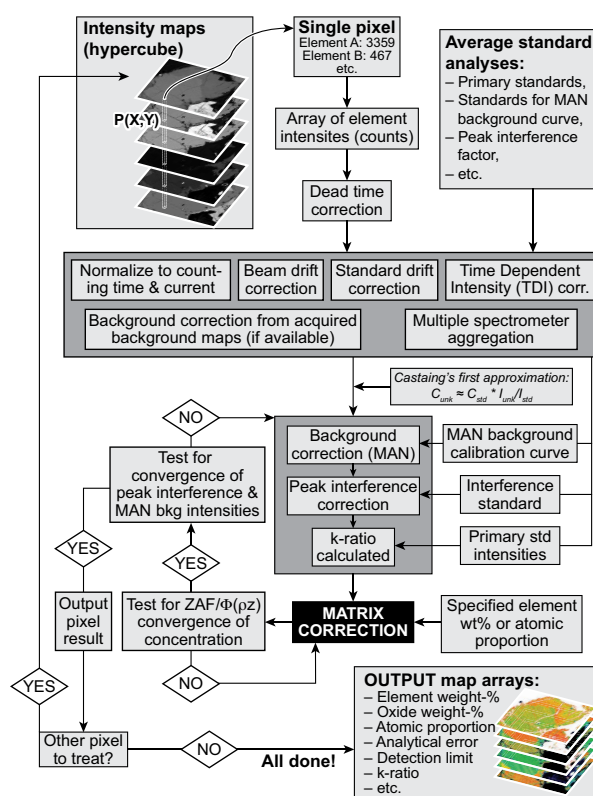

FIGURE 2. Flow chart of the proposed method for rigorously quantifying a series of raw intensity X-ray maps. These steps include normalization for pixel integration time, detector dead time, beam drift and standard drift (and optional off-peak map background corrections, TDI corrections and duplicate element aggregations), followed by iterative corrections for MAN background, matrix and spectral interferences on each pixel individually.

where i_{dt} = dead time corrected intensity, τ = dead time constant in seconds, i_{cps} = intensity in cps.

Second, divide the total X-ray intensities in both the standard point measurements and the unknown pixel measurements, by their respective integration times and beam currents to obtain counts per second per nanoamp (cps/nA) intensities (Eq. 2).

$$i_{cps/nA} = i_{counts}/(t \cdot nA) \tag{2}$$

where $i_{cps/nA}$ = normalized intensity in counts per second per nanoamp, i_{counts} = number of total raw X-ray intensity measured, t = counting integration time in seconds, nA = beam current in nanoamps (measured or interpolated).

The beam current values utilized for the standards are the measured beam currents from the standard intensity point measurements, while the beam current values for the map pixels are the interpolated beam currents measured prior and subsequently to the pixel intensity mapping measurements (see below for details).

Correction for beam drift and standard drift

Corrections for drift of the electron beam current are generally applied to the quantification of X-ray maps due to the frequently

extended acquisition times, even for modern instruments with beam current regulation. This beam drift correction is usually based on the beam current measurement before and after each map acquisition and is normalized to the X-ray intensities for each pixel based on the elapsed time between these beam current measurements. See Equation 3, which assumes the (slow) increment step motion is in the y-axis direction. Other beam drift correction methods include measuring the beam current before and after each scan line, although this procedure may not be necessary for modern instruments when the total map acquisition time is <10 or 20 h.

$$nA_{\text{Interpolated}} = nA_{\text{Start}} + \left(nA_{\text{End}} - nA_{\text{Start}}\right) * \frac{\left(P_x + \left(P_y - 1\right) * P_x\right)}{\left(N_x * N_y\right)} \qquad (3)$$

where $nA_{\text{Interpolated}}$ = interpolated mapping beam current, nA_{Start} = starting mapping beam current, nA_{End} = ending mapping beam current, P_x = position of a pixel the x array dimension, P_y = position of a pixel the y array dimension, N_x = number of pixels in the x array dimension, N_y = number of pixels in the y array dimension.

Similarly, if standard intensities were measured before and after the X-ray map acquisition, a drift correction in the standard intensities can be applied (Eq. 4). This drift corrected standard intensity is calculated on an element-by-element basis for each pixel and is applied to the denominator of the k-ratio prior to the quantitative matrix correction.

$$I_S = I'_S + \left(I''_S - I'_S\right)\frac{\left(T_P - T'_S\right)}{\left(T''_S - T'_S\right)} \qquad (4)$$

where I_S = interpolated (drift corrected) standard intensity, I'_S = standard intensity from the preceding standardization, I''_S = standard intensity from the following standardization, T_P = acquisition clock time of the X-ray map pixel, T'_S = acquisition clock time of the preceding standardization, T''_S = acquisition clock time of the following standardization.

Both the beam drift and standard intensity drift corrections assume linear drift in between beam current and standard intensity measurements, and of course are also dependent on the pixel acquisition order, which depends on the map acquisition (slow) step increment direction, and the instrument vendor as previously discussed.

Aggregate intensities for duplicate elements

Sometimes we need to improve the geometric efficiency of our photon collection by measuring the same element on multiple WDS spectrometers simultaneously (Donovan et al. 2011). Different spectrometer/crystal combinations can be used as long as the same X-ray line emission is utilized for each duplicate element. By aggregating intensities from several spectrometers, the analytical sensitivity and thus the detection limit can be significantly improved. The intensities for both the standard and the unknown are aggregated prior to the construction of the elemental k-ratio (see section "Trace elements and spectrometer aggregation" below for details).

Correction for X-ray continuum

WDS background (i.e., X-ray continuum) measurement is central to accurate quantitative microanalysis, especially for minor and trace elements. As mentioned previously, one or two background maps can be acquired to subtract the interpolated background from the on-peak map pixels at the cost of at least doubling the total mapping time. Alternatively, the mean atomic number (MAN) background method offers another background calibration method and provides several benefits for microanalysis, especially with regards to acquisition time and precision, particularly for X-ray mapping. Some investigators (Tinkham and Ghent 2005) have utilized a single MAN standard for X-ray map background corrections, but this is insufficiently accurate for maps containing multiple phases with different average atomic numbers. However, by measuring the X-ray intensity at the characteristic peak position for a given element on multiple standards (that do not contain the element), and which includes the range of average atomic number for the unknown phases to be mapped, we can create a robust relationship between these continuum intensities and average atomic number of these standards. Such MAN standard plots, usually acquired during the primary standard intensity calibration, yield an accurate WDS background calibration, provided that a correction for continuum absorption is properly applied to the measured intensities for each standard (Donovan et al. 2016).

The X-ray intensity data collected for these MAN plots are generally acquired at the same conditions as any other standard acquisition, and therefore have a precision that is equal to that for conventional spot analysis. For compositional mapping applications, the MAN background correction also provides an accurate background calibration that is used for all pixels in the map and at a precision that is superior to the counting statistics of conventional "off-peak" acquired background maps. In most silicate and oxide materials, the absolute accuracy of the MAN background correction is typically around 200 to 300 ppm, which is usually smaller than the expected precision of most X-ray map pixel intensities. The greatest benefit of the MAN background method is that all counting time in the mapping run is dedicated to the measurement of the characteristic X-ray peak, which significantly improves the precision and detection limit of the element (Donovan et al. 2016). Since the MAN method is more time efficient and actually provides better sensitivity, it is generally the preferred method for background correction of X-ray maps. Although MAN background calibrations might be slightly less accurate than using off-peak maps for background corrections, for example, when phases contain unanalyzed (or unspecified) elements such CO_2 in carbonates (depending on the details of the differences in average atomic number), utilizing MAN background-corrected X-ray maps does reduce the necessity for repeated map acquisitions, thus also reducing concerns regarding stage reproducibility and instrument stability. In addition, accuracy is further improved because the MAN background method completely avoids the problem of spectral interferences on off-peak intensity measurements from other emission lines since these off-peak intensities are no longer acquired when utilizing the MAN method. Finally, if necessary, a blank correction (Donovan et al. 2011) can be applied to the X-ray maps, if the map matrix is suitable, for even better accuracy.

Correction of spectral interferences

Correction of spectral interferences are applied to the pixel on-peak intensities during the matrix correction iteration based on the concentrations of the interfering elements (Donovan et al. 1993). This correction must be done iteratively with the matrix correction (Fig. 2; Eq. 5) as the interference correction can

change the composition of the pixel significantly enough so that the matrix correction must be recalculated based on the newly recalculated concentrations of all elements; this is even more important when considering mutual interferences of two analyzed X-rays (e.g., Ti$K\beta$ interferes with V$K\alpha$, and V$K\beta$ interferes with the trace levels of Cr$K\alpha$ in Al-Ti-V-Cr alloy).

$$C_A^u = \frac{C_A^S}{[ZAF]_{\lambda_A}^S}\,[ZAF]_{\lambda_A}^S\,\frac{I^u(\lambda_A)-\dfrac{[ZAF]_{\lambda_A}^{\bar{S}}}{C_B^{\bar{S}}}\dfrac{C_B^u}{[ZAF]_{\lambda_A}^u}\,I_B^{\bar{S}}(\lambda_A)}{I_A^{\bar{S}}(\lambda_A)} \quad (5)$$

where C_i^j = concentration of element i (A = measured element; B = interference element) in matrix j, $[ZAF]_{\lambda_i}^j$ = ZAF or $\Phi(\rho z)$ correction term for matrix j at λ_i for element i, $I_i^j(\lambda_i)$ = measured X-ray intensity in matrix j at wavelength λ_i, u = unknown sample, which contains elements A and B, S = primary standard, which contains only element A, $\bar{S}$ = interference standard, which contains a known quantity of the interfering element B, but none of the interfered with element A.

When necessary, this quantitative spectral interference correction routine is applied to each pixel of the acquired maps (and the standard point analysis intensities also), providing of course that the X-ray intensities of both the measured and the interfering elements are available.

Correction of time dependent intensity effects

Correction of time-dependent intensity (TDI) effects, such as alkali-migration in glasses due to beam damage (cf. Nielsen and Sigurdsson 1981; Morgan and London 1996), is quite straightforward for point analysis, as it simply requires the acquisition of "sub-interval" intensities during the on-peak measurement to monitor and correct for a change in count rate over time. The same principle can be applied on beam mapping: by acquiring multiple frames of X-ray maps, we can obtain an evolution of the count rate for each pixel over time and thus correct for possible changes in X-ray intensity by extrapolating back to the intensity at time zero using Equation 6.

$$I_C = e^{\log(I_R)-m\cdot t\cdot 0.5} \quad (6)$$

where I_R = X-ray intensity in counts per second per nA, m = time dependent intensity (TDI) slope coefficient from linear fit of log intensity vs. time, t = total elapsed integration time.

Linear, quadratic, or logarithmic TDI fitting models can be applied on an element-by-element basis; quadratic or logarithmic corrections are often necessary for extremely beam sensitive materials (von der Handt in preparation).

Correction of compositional matrix effects

Once the k-ratios for each element are calculated from the normalized and background corrected unknown map pixel and standard point intensities, a matrix correction can be applied. Selection of the proper matrix correction routine is out of the scope of this paper, and the analyst will be the judge of that choice. Typical analytical physics models can be used [e.g., ZAF or $\Phi(\rho z)$] or even Monte Carlo methods (Donovan 2019). In general, quantitative analysis using the electron microprobe is generally based on Equation 7:

$$C = k\cdot[ZAF] \quad (7)$$

where C is the concentration result, [ZAF] is the total matrix correction, including the standard k-factor correction for when the standard is not a pure element (e.g., Armstrong 1988), and k is the raw k-ratio intensity expressed as $I^{sample}/I^{standard}$, where I are the continuum corrected peak X-ray emitted intensities measured on samples and standards, respectively. Modern matrix correction algorithms correct for electron energy-loss and backscattering in the atomic number factor Z, absorption of characteristic X-ray intensities in the absorption factor A [both of which are combined in $\Phi(\rho z)$ matrix correction methods], and additional X-ray intensities resulting from characteristic (and ideally continuum) X-ray fluorescence in the fluorescence factor F. This matrix correction is made iteratively using a refined estimate of the pixel concentration. The final analysis result is identified when no further improvement in the concentrations is obtained, just as in the case of single-point analysis. In fact, we utilize the same source code for both point analysis and map pixel analysis in all our results.

Additional corrections for soft X-rays

Not discussed in this paper are the effects of changes in peak shape on soft X-rays and the correction algorithm using area peak factors (Bastin and Heijligers 1991). This approach is applied for the accurate quantification of low-atomic number emitters. However, due to the chemical bonding dependency of such corrections, they are of limited use in X-ray mapping when multiple phases are present. Nonetheless, it should be mentioned that the choice of different matrix correction models and mass absorption coefficients can have significant effects on the accuracy of quantitative results and should be considered when performing quantitative X-ray mapping with highly absorbed emission lines, such as low-atomic number K-lines or other very soft X-ray emission lines, e.g., L-lines of first-row transition elements.

Computation time and complementary calculations

The processing of a typical set of 10 element X-ray maps of 512 × 512 pixels will require tens of minutes to a couple hours of matrix physics calculation time depending on the speed of the computer; most modern computers will process the data of smaller maps with fewer elements in <10 min. Elemental concentrations, along with background-, net-, and k-ratio intensities, are generally calculated by default. An analytical total weight percent map is also usually calculated to further help in judging the data quality. In addition, other information can be mathematically extracted from the elemental concentration data, such as oxide weight percent, atomic proportions, formula basis calculations, and logarithmic wt% of concentrations for trace element mapping. Statistical data such as detection limits and analytical sensitivities can also be calculated for each pixel as well. Optionally, and if appropriate for the compositions in question, several other map data can be extracted, such as a stoichiometric oxygen map, an excess oxygen map (from assumed oxygen stoichiometry and/or measured anions such as F and Cl), and a map of an element calculated by difference from 100%. To facilitate the calculation of all specified output types, it is more efficient to calculate them during the map quantification, although they can be easily recalculated using the primary output (elemental wt%).

Because all pixels during the quantification of X-ray maps are treated to the same matrix correction methods as we traditionally perform for point analyses, very large maps with many elements can require considerable time for the calculation of concentrations. The calculation timescales linearly with the number of pixels and exponentially with the number of elements analyzed. The fully automated processing of these quantitative maps can be done off-line on any computer without any action from the user besides the selection of the appropriate quantification parameters [e.g., choice of primary and interference standards, definition of the MAN background curves, calculated elements (by stoichiometry, by difference, etc.)]. All maps presented in this paper followed the procedures as presented above and were performed using the Probe Software Probe for EPMA and CalcImage software packages (https://probesoftware.com/), though other software codes could perform similar quantitative corrections to raw X-ray map intensity data.

Results and Discussion

Primary standards required for quantitative mapping are usually acquired as point analyses at a moderate beam current (typically 10–50 nA) with integration times of 10–30 s. However, stage or beam scanned X-rays maps are usually acquired at higher currents, typically 20 to 500 nA, even 1 µA in cases of trace element mapping, and using a pixel dwell time on the order of tens to hundreds of milliseconds or more per pixel (which makes it essential that the actual beam currents be recorded for both the standards and the X-ray map acquisitions in real-time). Since both time and beam current should scale proportionally, doubling the count time is equivalent to doubling the beam current (ignoring dead time effects). To compare data and evaluate the precision of each measurement, the total electron dose (i.e., the product of beam current and time) should be considered. Ignoring the effects of electron beam energy in beam power calculations, we can simply say that single-point analyses, for instance in standards, typically yield a total electron dose in the range of 100 to 3000 nA·s. Quantitative element maps runs typically utilize higher currents (20–500 nA) to compensate for shorter count times (20–1000 ms), which translate to a dose range of 0.4 to 500 nA·s per pixel. In other words, even well-chosen conditions for element maps can still represent an electron dose several orders of magnitude less than for single-point quantitative analysis. This dose should be carefully considered with regards to the beam size, and the applied dose should be normalized to the impacted surface (i.e., expressed as nA·s/µm^2). This calculation of electron dose is useful for evaluating the precision and detection limit for conventional single-point vs. map-pixel analysis and reveals that mapping measurements usually have lower precision and, therefore, higher detection limits at each individual pixel (Carpenter and Hahn 2017). It is therefore legitimate to ask how precise and accurate quantitative element mapping truly is. Calculation of the electron dose can also be useful to evaluate the maximum allowable dose for beam-sensitive materials before beam exposure damages the sample too much, resulting in inaccurate results. In such cases, large area stage mapping is often done with a relatively large beam size that matches the pixel size to further assist in dissipation of the electron dose over a large area, thus minimizing the problem of beam damage.

Evaluation of accuracy

It is not immediately obvious that X-ray maps acquired using a dwell time per pixel of a few hundred milliseconds or even less can be accurately quantified due to the apparently poor counting statistics per pixel. But accuracy depends primarily on matrix corrections, background and peak interference corrections, standard reference values, etc. All these parameters remain the same whether a single-spot analysis or quantitative element map pixel is considered, and therefore the map-derived element concentrations should be just as accurate as a single point measurement, with the caveat that the absolute accuracy of the pixel dwell times (for both "continuous" and "step" mapping modes) at the millisecond level should be verified by both the instrument vendor and user, for best quantitative mapping accuracy. In addition, when the primary standards and X-ray maps are acquired at significantly different beam currents, the linearity of the beam current nano-ammeter is critical for best accuracy, not to mention the importance of the WDS detector dead time calibrations when high-X-ray intensities from high-mapping currents are combined with standard intensities acquired with lower beam currents for the primary standard calibrations, in the subsequent construction of the raw k-ratio prior to quantification.

In any case, all quantitative measurements require an average and a variance regardless of whether this is for point or pixel measurements. Similar to point analyses, a representative sampling of the specimen composition requires the examination of an average and standard deviation of each set of points or of pixels, especially in multiphase materials.

To demonstrate the accuracy of the proposed quantitative mapping approach, a simple X-ray map in the reference glass material NIST K-411 is quantified (Fig. 3). For this example, element maps were acquired using a Cameca SX-100 electron probe microanalyzer at CAMCOR (University of Oregon), using analyzing crystals LIF for FeKα, PET for SiKα, LPET for CaKα, TAP for AlKα, and LTAP for MgKα. Analytical conditions were 15 keV, 30 nA using a 128 × 128 pixels stage scan with a pixel dwell time of 500 ms and a pixel size of 0.5 µm. Results of the quantification process are given in Figure 3. In this map quantification, oxygen was calculated by stoichiometry with an additional 1.12 wt% oxygen from ferric iron (as determined from colorimetry). All maps are corrected for background using the MAN background correction. The calculation of a total concentration map (g) provides for evaluation of the analysis accuracy as all elements should total close to 100%. The calculated quantitative pixel average results are subsequently compared to NIST published values (Table 2). Excellent accuracy is achieved as the calculated weight percent of all four major elements (Si, Mg, Ca, and Fe) are statistically equivalent to the certified NIST values, and Al accurately yields a zero-value (nominally Al-free glass).

Evaluation of precision

The shorter pixel integration times of X-ray mapping compared to point analysis generally leads to poorer Poisson statistics. Therefore, the apparent precision per pixel is more limited, and it should be evaluated carefully. Mapping precision and sensitivity are considerably improved by pixel averaging, as it is commonly done for multiple point measurements in a homogeneous area or by kernelling or binning such as it is already done,

TABLE 2. Comparison of the average of all map pixels with published reference values for NBS K-411 mineral composition glass from NIST

	Si wt%	Fe wt%	Mg wt%	Al wt%	Ca wt%	O wt%	Calc. O	Total
Average	25.06	11.18	8.63	0.02	10.98	1.12	42.93	98.80
Published	25.38	11.21	8.85	n.a.	11.06	1.12	43.56	99.98
St.dev.	0.72	0.64	0.15	0.02	0.20	0.00	0.86	1.84
Rel %	2.89	5.74	1.75	99.23	1.85	0.00	2.01	1.86
Minimum	22.28	8.43	8.06	−0.05	10.16	0.00	39.56	91.77
Maximum	27.84	14.17	9.25	0.13	11.82	0.00	46.38	106.08

Notes: The standards were MgO synthetic for Mg$K\alpha$, SiO$_2$ synthetic for Si$K\alpha$, and NBS K-412 mineral composition glass for Fe$K\alpha$, Al$K\alpha$, Ca$K\alpha$. n.a. = not analyzed.

for instance, with EDS maps. Such pixel averaging can provide enough precision for discriminating small differences in concentrations and can ultimately increase the analytical sensitivity.

Table 3 compares point analyses (average of 4 points) of standard material NIST K-411, with pixel averages from the quantitative X-ray map (Fig. 3), using pixel aggregates from 4 to 64 pixels. Comparing pixel averages with point averages reveals that accuracy and standard deviation (pixel variance) are consistent and in close agreement with the average and variance of 4-point averaged measurements. Naturally, the error of the

mean or standard error (pixel error) improves significantly with the number of pixels being averaged (Table 3).

Bad pixels

When considering pixel averaging in an unknown sample, we must also consider the adverse effects from so-called "bad pixels" that can degrade our quantitative maps with inaccurate data. A bad pixel is often the consequence of breaking one of the essential requirements of WDS measurement (flat and horizontal surface, homogeneous domain, proper working distance, etc.) or a hardware issue (e.g., sudden beam current instability, noise on a WDS X-ray detector, etc.). Excluding hardware problems, a typical bad pixel is commonly due to surface defects (holes, cracks, poor polishing, etc.), phase boundaries (Barkman et al. 2013), or finely intergrown materials or exsolutions. The choice of beam diameter and accelerating voltage along with the density of the analyzed phase will control the size of the analyzed volume. When a larger analytical volume is considered, a higher number of bad pixels is to be expected, especially when the average grain size or feature to be mapped is approaching the size of the analytical volume. In other words, the larger the analytical
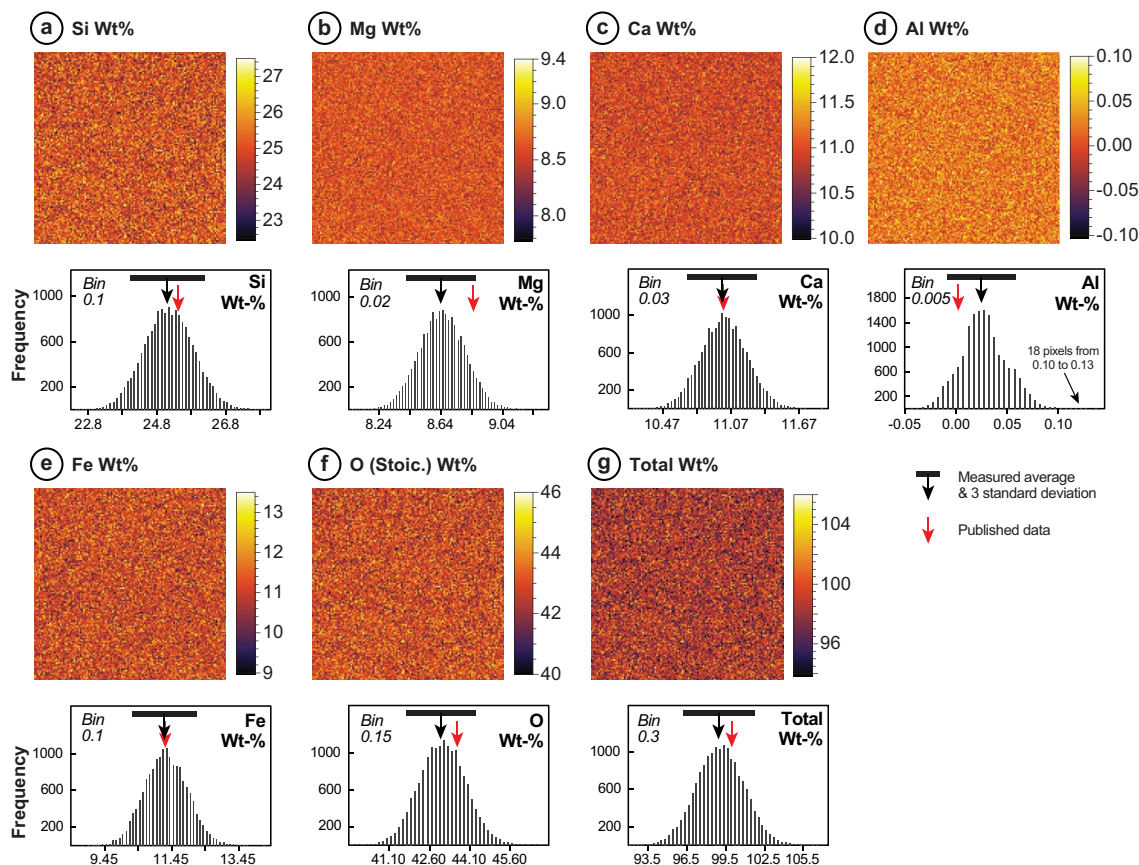

FIGURE 3. Quantified elemental X-ray maps for Si$K\alpha$, Fe$K\alpha$, Ca$K\alpha$, Al$K\alpha$, and Mg$K\alpha$ for the NIST K-411 silicate glass reference material, with a total weight percent map and an oxygen map calculated by stoichiometry with an additional 1.12% O to account for the presence of ferric iron, shown along with quantitative histograms and measured average and 3 standard deviation bar and certified values for each element (in red). Conditions were 15 keV, 30 nA, and 500 ms per pixel. Field of view is 63.5 × 63.5 μm. Note the analytical total map, which is important just as it is for point analysis. These simple maps demonstrate that mapped pixels can achieve accuracy similar to normal point analyses, even though single pixel precision can be problematic without pixel averaging as seen in the map color scale ranges. See Table 3 for a numerical summary.

volume and/or the smaller the phase dimensions, the greater the number of pixels compromised by edge, crack, and mixed-phase interaction volumes. Large well-polished phenocrysts might give overall excellent results, but a fine-grained heterogenous matrix may not. For this reason, the best approach would utilize a focused beam, despite the fact that this would increase the current density and potential for beam damage. The key point is to constrain the analytical volume and the pixel size to ultimately obtain a representative number of pixels for the smallest feature to be mapped while minimizing the number of bad pixels.

When considering pixel averaging, including "bad pixels" in the average can affect both the precision and the accuracy. Therefore, the use of pixel extraction and filtering methods are recommended and available in many image processing programs (e.g., Probe Software CalcImage, NIH ImageJ, etc.). This approach allows the analyst to specify the exact pixel area to be extracted from the map by providing for instance, a pixel filtering based on quantitative compositional limits for selected analyzed elements. In this way one can avoid and/or filter out these bad pixels from our compositional averages. An example is provided later in this paper.

Quantitative mapping results

Geologists and materials engineers commonly require detailed element mapping of complexly zoned phases. Whereas point analysis yields very precise and accurate data, it commonly fails at revealing all the subtleties of compositional zonation (if present). Mapping is therefore necessary, and as discussed above, both precision and accuracy can be obtained depending on the analytical settings and the pixel averaging employed.

As a first example, a simple mapping of plagioclase with five major elements (Si, Al, Ca, Na, and K) is considered. The sample is from the Adamello tonalite in Northern Italy (Fiedrich et al. 2017), and shows strong compositional zoning from an inherited anorthite-rich core to an albite-rich rim overgrowth showing significant oscillatory zoning. After performing the quantitative calculations for each pixel, the fully quantitative elemental or oxide weight percent (wt%) concentrations are available for output (Fig. 4a). In addition, these elemental concentrations can be expressed in any number of various output types, such as atomic percent or formula basis (Fig. 4b) and various end-member mineral normalizations. Additional normalizations based on the previously calculated elemental or molar concentrations can also be performed. For example, mineral end-member calculations where the Ca, Na, and K concentrations are normalized to produce maps of anorthite, albite, and orthoclase end-member components for each pixel in the original map (Fig. 4c), though multiple normalizations may be necessary when more than one mineral phase is present.

If a single phase is of interest to the researcher, pixel filtering and extraction based on chemical composition and the analytical total can be applied. In Figure 4d, only the pixels corresponding to a plagioclase composition are extracted; the conditions in this example are: $90\% <$ Total < 110 wt%, $40 < SiO_2 < 75$ wt%, $15 < Al_2O_3 < 40$ wt%, CaO < 25 wt%, $Na_2O < 15$ wt%, and $K_2O < 2$ wt%. This compositional filtering also allows us to remove any of the previously discussed bad pixel effects to improve accuracy. It is then possible to extract

TABLE 3. Evaluation of accuracy and precision for NIST standard K-411 by averaging various numbers of pixels from the quantitative X-ray maps compared to the average of 4 point analyses

	Si wt%	Al wt%	Fe wt%	Mg wt%	Ca wt%	Integration time
NIST K-411 (published)	25.38	n.a.	11.21	8.85	11.06	
NIST K-411 (measured)	25.277	0.019	11.098	8.811	11.037	80 s
4 points variance	0.037	0.004	0.082	0.027	0.025	
4 points error	0.019	0.002	0.041	0.014	0.013	
4 pixels average	25.261	0.021	10.893	8.741	11.289	0.4 s
4 pixels variance	0.582	0.050	0.409	0.528	0.510	
4 pixels error	0.291	0.025	0.205	0.264	0.255	
16 pixels average	25.432	0.000	10.996	8.947	11.112	1.6 s
16 pixels variance	0.507	0.038	1.293	0.584	0.500	
16 pixels error	0.127	0.010	0.323	0.137	0.125	
32 pixels average	25.399	0.011	11.131	8.747	11.049	3.6 s
32 pixels variance	0.454	0.046	1.444	0.589	0.406	
32 pixels error	0.076	0.008	0.241	0.098	0.068	
64 pixels average	25.463	0.016	11.310	8.809	11.046	6.4 s
64 pixels variance	0.529	0.044	1.563	0.670	0.414	
64 pixels error	0.066	0.001	0.195	0.084	0.052	
All pixels average	25.353	0.016	11.057	8.748	10.994	1638 s
All pixels variance	0.494	0.048	1.427	0.593	0.460	
All pixels error	0.004	0.001	0.011	0.005	0.004	

Notes: Values for pixel variance (standard deviation) are consistent, while the standard error (around the average) decreases, with increasing pixel count as expected. n.a. = not analyzed.

quantitative data using a pixel averaging of multiple pixels of similar composition to obtain a more precise measurement, such as discussed previously. It is also possible to work on other statistical data such as histograms of composition to delineate for instance, the modal abundance of an anorthite-rich core vs. an albite-rich rim (Fig. 4e).

It is also possible to calculate the detection limits and analytical sensitivity just as it is done for single point analyses (Fig. 5). At the analytical conditions considered here (50 nA, 50 ms per pixel), the per pixel calculated analytical sensitivity (~2–5% for major, >10–20% for minor element) and detection limit (typically between 0.06 and 0.15 wt% in this example) remains, of course, high, when compared to point analysis, but can be further improved through pixel aggregation or with longer counting time, higher beam current, or more optimal spectrometer selection (e.g., large area monochromator, P-10 vs. Xe counter). For cleanliness of the output, the analytical sensitivity calculations can be skipped for any pixel yielding a concentration <1 wt%, as it usually yields very high and meaningless values (gray pixels).

Comparing raw intensity maps to matrix effect corrected maps

Traditionally, raw intensity WDS and EDS X-ray maps were used for the documentation and interpretation of chemical variation in solid materials. For several decades, EDS X-ray maps have been quantitative (at least when standards are utilized) because it was relatively easy to do so. While the importance of matrix corrections in WDS spot analyses is universally acknowledged, lack of computing power and software development has posed a hindrance in extending robust corrections to WDS X-ray maps. However, in situations that require significant absorption correction for X-ray intensities, substantial discrepancies can be observed between raw and quantified maps. Figure 6 is one example of such a case, showing a Fe-Ti oxide grain with Fe-rich
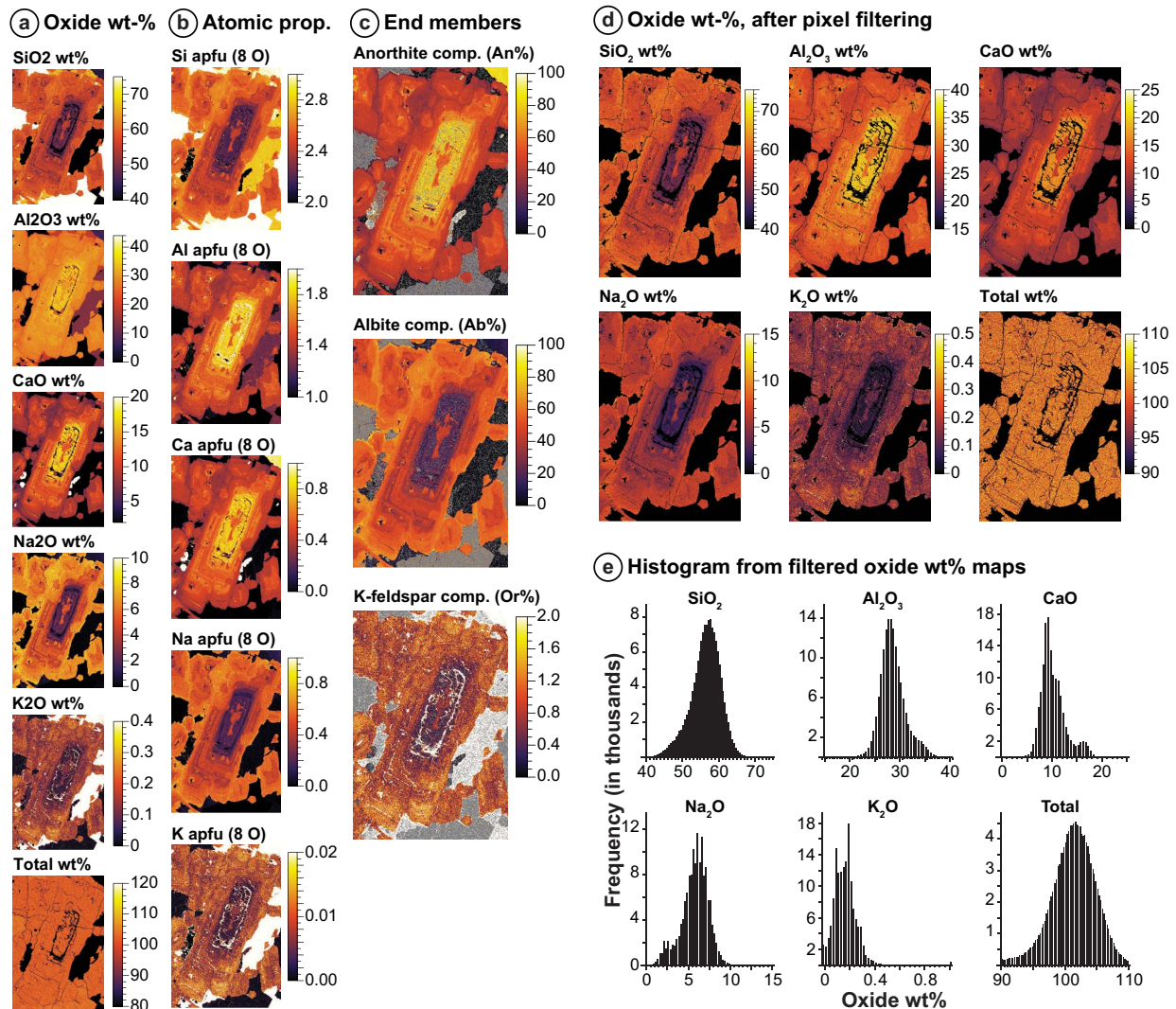
FIGURE 4. (**a**) Quantitative maps in oxide concentrations (wt%) for a feldspar grain from the Adamello tonalite; *K*α lines were analyzed for all elements. Oxygen calculated by stoichiometry (not shown here). Conditions were 15 keV, 50 nA, and 50 ms per pixel. Field of view is 1.11 × 1.644 mm at 3 μm/pixel resolution. (**b**) Formula basis maps for a feldspar grain based on 8 oxygen atoms (apfu = atoms per formula unit). (**c**) Recalculated mineral end-member maps: albite (Na), anorthite (Ca), and K-feldspar (K). (**d**) Pixel filtering based on compositional limits and analytical totals. (**e**) Quantitative histograms of the previous pixel filtered quantitative maps.

core and exsolutions of ilmenite ($FeTiO_3$) and titanite ($CaTiSiO_5$).

The raw X-ray map of oxygen (Fig. 6a) would suggest relatively constant oxygen contents across the mineral grain, while the fully quantified map (Fig. 6b) shows pronounced differences in oxygen concentrations. Maps of net and background intensities (Figs. 6c and 6d) calculated by MAN show a slight increase in background intensities in the core but a negligible difference in net counts due to the high peak-to-background ratios for oxygen across all phases. Therefore, neither a background-corrected map by itself, nor a quantification using a calibration curve, would accurately reveal the varying oxygen contents.

In this example, emitted O*K*α X-ray intensities in the Fe-Ti oxides are dominantly controlled by the changes in mass absorption of O*K*α by Fe, Ti, or O itself. Mass absorption coefficients

for O in Ti and Fe, respectively, differ by almost an order of magnitude (Ti: 22 422 vs. Fe: 3625; FFAST database; Chantler 2000; Chantler et al. 2005). Consequently, for a given oxygen wt% content, areas high in Fe will show higher relative O*K*α intensities, whereas Ti-rich areas will show lower X-ray intensities as they will be absorbed more. Only a full quantification, including a background and matrix correction (and interference correction), can adequately account for this change in X-ray emission rates. It is therefore essential that the analyst rigorously quantify each pixel using the methods described in this paper so that they can be confident that differences in concentrations and zoning are not masked or introduced by variations in background intensities, absorption, and fluorescence effects between grains or mineral domains.
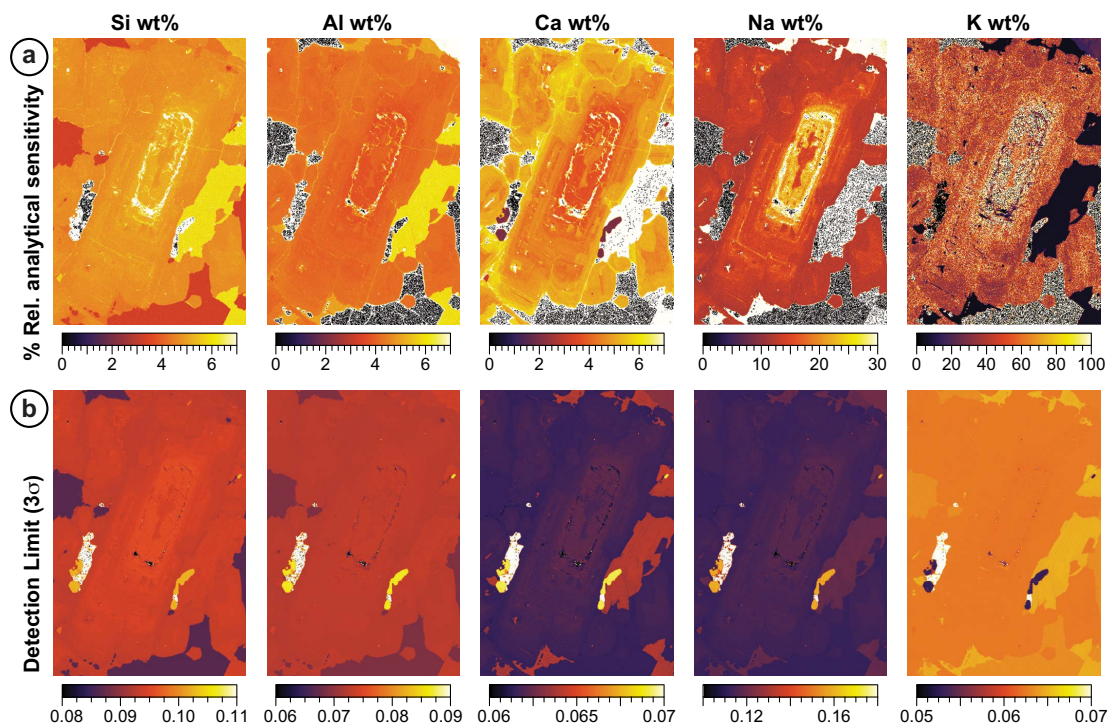
FIGURE 5. Maps of the (**a**) relative analytical sensitivity (1σ), and (**b**) detection limit at 99% confidence (3σ) for Si, Al, Ca, Na, and K calculated for each individual pixel for a feldspar grain from the Adamello tonalite.
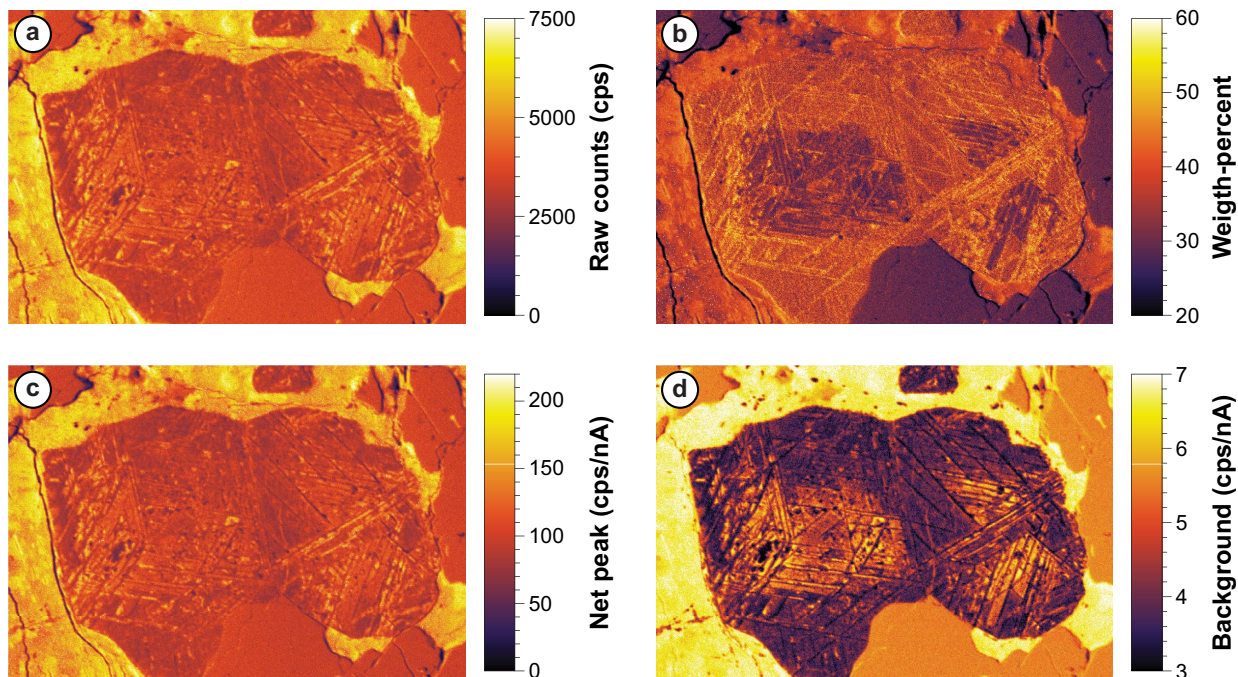

FIGURE 6. Element maps of a Fe-Ti mineral from the mafic-ultramafic Viravira Complex, Colombia. Conditions were 8 keV, 35 nA, and 100 ms per pixel. O$K\alpha$ measured on LDE1 monochromator, and PROZA91 matrix correction was applied with MAC values from FFAST database. Field of view is 414 × 274 μm. (**a** and **b**) The raw intensity X-ray map of O$K\alpha$ (**a**) in the Fe-Ti-oxide mixture shows significant differences when compared to the fully quantified X-ray map (**b**). (**c** and **d**) While the map of the calculated background intensities (**d**) correlates with Fe-rich core areas, the net intensities (**c**) are not affected due to the high-peak-to-background ratios.

Trace element quantification in X-ray maps

Rigorous quantification is essential to facilitate accurate evaluation of X-ray intensity maps of elements with trace concentrations (<1000 ppm). The crucial point for accurate trace analysis is the correction for the X-ray continuum contribution to the measured X-ray intensity at the Bragg conditions for the characteristic X-ray of interest (see Jercinovic et al. 2012; Allaz et al. 2019a) because continuum intensity varies as a function of the mean atomic number of a given phase, and also from absorption effects associated with the composition of the phase. An accurate EPMA trace element analysis, whether it is by single point analysis or by pixel mapping, can only be accomplished with an accurate and precise background correction. This means that the continuum must be accurately calculated or measured, for each pixel, with a precision sufficient to answer the analytical questions at hand.

Bremsstrahlung correction can be problematic for multiphase element mapping, where each phase has a potentially different average atomic number. It can also be problematic for a single phase that displays a significant compositional zonation inducing a significant change in average Z-number (e.g., Z-bar ~10.7 to 11.9 between albite and anorthite). This issue gets even more complicated when multiple substitutions are possible in a strongly heterogeneous phase and when both light and heavy elements are substituting (e.g., in zircon: Zr ↔ [Hf,U,Th], Si+Zr ↔ P+REE, etc.).

As previously described, when acquiring EPMA trace element point measurements, typically the background X-ray intensity is sampled by de-tuning each WDS spectrometer to both the high and low sides of the characteristic X-ray peak, implying at least a doubling of the acquisition times. Fortunately, we can also apply the MAN background correction to X-ray maps, just as it is applied to point analyses. Once a MAN background calibration curve is defined for each element to be mapped, there is no need to measure a background map.

Figure 7 compares the quantification of trace element maps of Hf$L\alpha$, Y$L\alpha$, P$K\alpha$, U$M\alpha$, and Th$M\alpha$ in zircon using off-peak
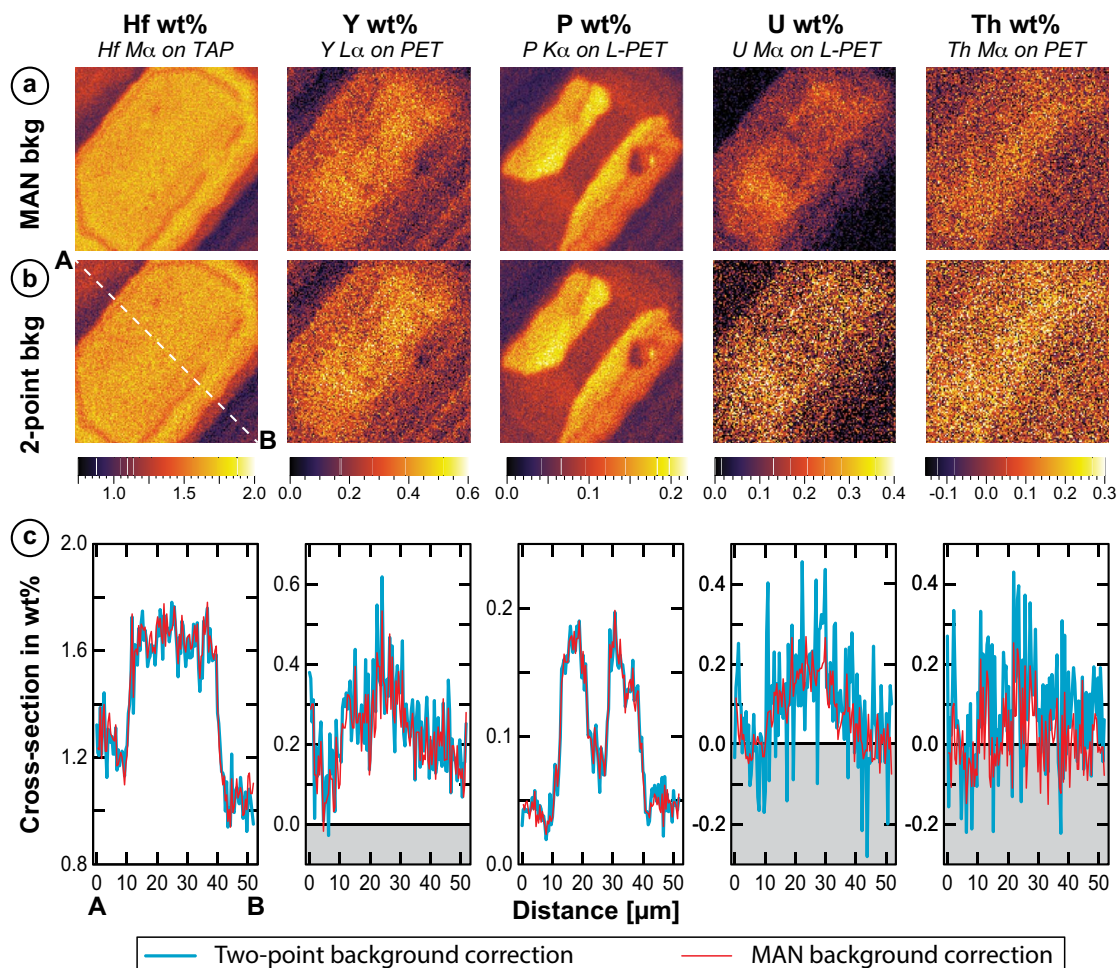

FIGURE 7. Quantitative X-ray maps of trace elements in a zircon grain using off-peak maps for the interpolated off-peak background map correction (**a**), and alternatively using MAN background corrections (with the same on-peak map intensities) in **b**. Conditions were 15 keV, 100 nA, and 1800 ms per pixel (on-peak and total off-peak). Field of view is 38.1 × 38.1 μm. Three separate map scans were acquired: the on-peak intensity maps, followed by the high-off-peak intensity maps, followed by the low-off-peak intensity maps. A comparison of the off-peak and MAN maps are seen in the cross sections for each element (**c**). Note the improvement in precision particularly for U and Th cross sections with the MAN corrected maps (red lines) compared to the off-peak corrected X-ray maps (blue lines).

map acquisitions (employing two WDS spectrometer positions with a linear interpolation of the off-peak map pixel intensities), and also using the MAN background correction, with both methods utilizing the same on-peak map intensities. The ZrO_2 and SiO_2 contents were constrained by assuming a mineral formula by difference from 100%. This is accomplished by including the calculated $ZrSiO_4$ (by difference from the measured elements) into the matrix correction during the matrix iteration calculations so that an accurate matrix and average atomic number (for the MAN interpolation) is obtained. In addition, it should be noted that a correction for the interference of Th$M\beta$ on U$M\alpha$ should normally be applied. However, in this example, the Th content is barely above detection limit, and therefore a spectral interference correction is unnecessary in this particular case.

Somewhat unintuitively, the use of MAN background calibrations actually improves precision because the background intensity calculation is no longer limited by continuum statistics but is instead based on our major element concentrations, which solely determine the average atomic number of the matrix, and hence the precision (and accuracy) of the absorption-corrected MAN background curve. Both background correction routines yield equally accurate results, yet the MAN background-corrected maps (Fig. 7a) yields more precise results with less noise (especially visible on U and Th maps). These MAN background calibrations can result in accuracy errors for trace elements on the order of a few hundred ppm in typical geological materials, although this can be accurately compensated for by the use of the "blank" correction (Donovan et al. 2011). However, the pixel level measurement precision in our X-ray maps is limited by the pixel dwell time (and beam current), and in most situations, it is significantly worse than the accuracy obtained with the MAN background correction.

Even with a cursory visual examination of the off-peak and MAN background-corrected trace elements maps, the MAN-corrected quantitative element maps clearly provide improved precision/sensitivity compared to the off-peak background-corrected maps, without the need of doubling or tripling the acquisition time to obtain background maps. Another advantage of the MAN correction is that it reduces the risk of acquiring a background map at a wavelength (off-peak) position that could be interfered with by another major or minor element present only in a few phases or in a specific zone of the area to be mapped.

The higher sensitivity seen in the MAN background-corrected maps is due to the fact that when the on-peak intensities are corrected for background, the variances of the on and off-peak intensities are added in quadrature:

$$\sigma_{P-B} = \sqrt{\sigma_P^2 + \sigma_B^2} \qquad (8)$$

In practice, this means that as the measured concentration approaches zero, and therefore the variances of the on-peak and off-peak become similar, the precision of the background intensity becomes as important as the precision of the on-peak measurement. In a classical two-point background acquisition, the error on the two-background measurement is limited to only continuum counting statistics, which due to the relatively low intensity, results in a relatively low-precision background correction. On the other hand, because the error on a MAN-calibrated background correction is limited primarily by the measurement precision of the major elements (e.g., the variance of the average atomic number of the material from the high-concentration elements), the variance of the interpolated background intensity is much smaller (see Donovan et al. 2016 for a discussion of these statistical considerations). In fact, typically the resulting precision of the MAN net intensity background is ~40% better than traditional off-peak corrections (by the square root of two), because the background variance term in Equation 8 (σ_B^2) approaches zero, particularly when the major matrix elements are specified by difference or fixed concentration). Therefore, it is primarily only the precision of the on-peak measurement term (σ_P^2 in Eq. 8), which contributes to the net intensity precision when the MAN background method is utilized.

Correction of spectral interferences in X-ray maps

Correction of spectral interferences is also particularly critical for accurate quantitation of trace elements where a trace element X-ray emission line is overlapped by a significant emission line from another element. This problem is illustrated by obtaining X-ray maps for S$K\alpha$, Fe$K\alpha$, Cu$K\alpha$ (Figs. 8a–8c), and Mo$L\alpha$ (Figs. 8d–8f) from a sample containing the phases pyrite (FeS_2) and chalcopyrite ($CuFeS_2$). These maps are followed by the extraction of a cross-section A–B across the pyrite-chalcopyrite interface (Figs. 8g and 8h). The Mo contents of both sulfides are expected to be at the trace level, most likely below the detection limit of the map measurement sensitivity. Yet, the raw counts (Fig. 8d) apparently reveal the presence of significant Mo. This apparent Mo signal mostly comes from the strong interference of Mo$L\alpha$ by S$K\alpha$ on a PET monochromator, and therefore a correction for spectral interference is essential for Mo accuracy. Without a peak interference correction (Fig. 8e), up to 1.8 and 1.2 wt% Mo is erroneously measured in pyrite and chalcopyrite, respectively. When a quantitative interference correction is applied (Donovan et al. 1993), data essentially yield values at or below detection limit (~700 ppm at the mapping conditions utilized), as seen in Figure 8f.

Interestingly, visualization of the spatial distribution of an element that has a large compositional range can also be problematic. For example, the Cu element map in Figure 8c shows levels of Cu approaching zero in pyrite (phase on the left), but around 33 wt% in chalcopyrite (phase on the right). One solution to this visualization problem is the use of logarithmic weight percent values to scale the element map. Figure 9 shows the application of a logarithmic scale to the Cu wt% values and subsequently elucidates an apparent increase in Cu up to ~1 wt% in pixels adjacent to the chalcopyrite boundary (Fig. 9b); an observation that otherwise might have been missed. In this specific example, the apparent presence of Cu at the grain boundary is not related to diffusion but is instead an artifact from the secondary fluorescence effect from the bremsstrahlung (e.g., Borisova et al. 2018).

Quantification of beam sensitive samples or TDI scanning

The electron beam can cause many materials to suffer from ion diffusion, recrystallization, amorphization, or even volatil-

ization (e.g., loss of OH, H_2O, or CO_2 groups) chiefly due to the heat (phonon excitation) generated by incident electron interaction with matter (Hughes et al. 2019). In such cases, where the beam current cannot be reduced or defocused, and a high thermal conductivity coating (e.g., Al, Ag, or Ir) is not appropriate, it is recommended to apply a time-dependent intensity (TDI) correction that can account for the ion migration and/or a change in signal due to physical changes in the analyzed material, provided it follows a linear, exponential, or polynomial trend over time. These so-called beam sensitive materials can be extremely dif-

Quantitative maps (element wt%)

Raw image Mo Kα in cps   *No interference correction*   **With interference corr.**
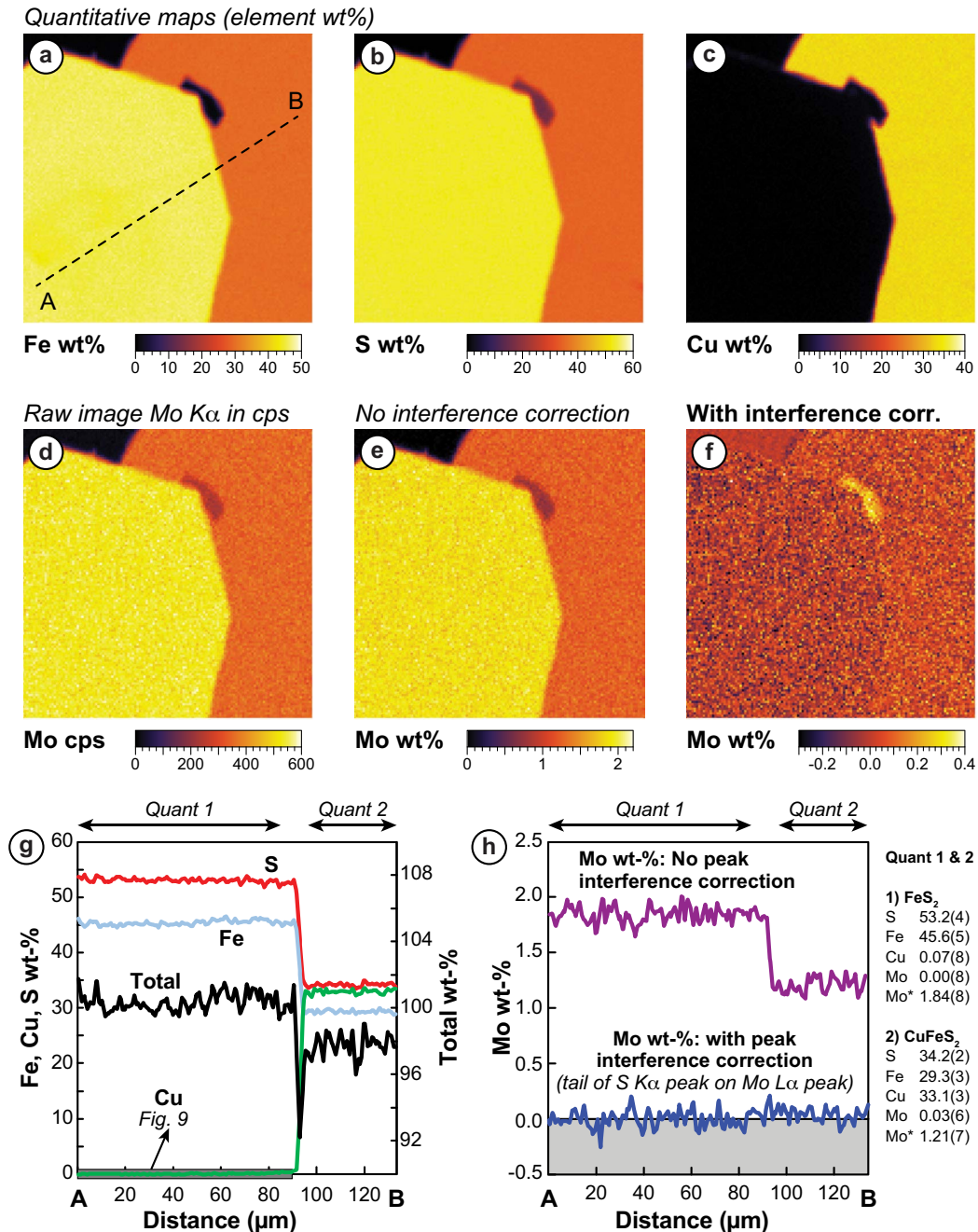
FIGURE 8. (**a–c**) Quantitative element maps of Fe, S, and Cu. Conditions were 15 keV, 100 nA, and 1000 ms per pixel. Field of view is 127 × 127 μm. (**d**) Raw X-ray map of MoLα expressed as counts per second, (**e**) quantified X-ray map without a spectral interference correction, and (**f**) with interference correction. (**g** and **h**) Cross section A–B across the pyrite-chalcopyrite interface with and without a spectral interference correction. (**g**) Major element values are within the range of expected values for pyrite and chalcopyrite. Totals are very close to 100% in pyrite and slightly lower in chalcopyrite most likely due to the presence of minor elements not analyzed. (**h**) Comparison of the Mo content with (Mo) or without (Mo*) the peak interference correction. Numerical data on the right side are average of concentration measurements along the profile (see "Quant 1" and "Quant 2" aside the profile). Error (1σ) indicated in parentheses.
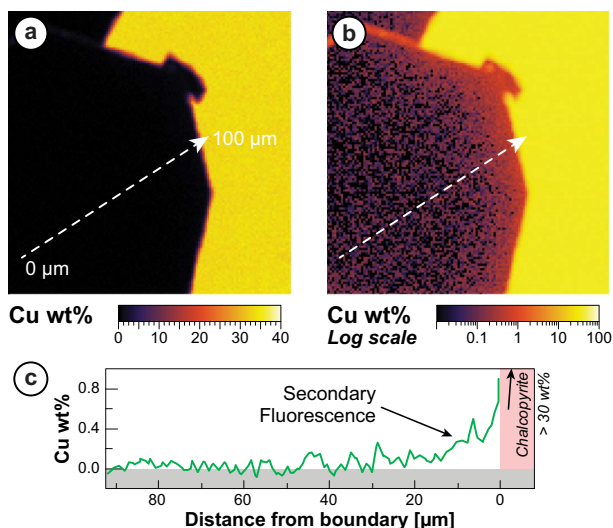
FIGURE 9. Comparison of Cu element wt% map shown with (**a**) a linear or (**b**) a logarithmic scale. Using the logarithmic scale, the spurious low concentrations of Cu in pyrite due to secondary fluorescence across the phase boundary can be made visible, while avoiding oversaturation of pixels with higher Cu content in chalcopyrite. (**c**) Plot of Cu wt% in pyrite vs. the distance to the boundary with chalcopyrite.

ficult to analyze using single-point analysis due to the limited analytical time available before the material is so badly damaged that even a TDI correction cannot account for the change (e.g., Allaz et al. 2019b).

Among the classic examples in the literature are, for instance, phosphates (e.g., Goldoff et al. 2012; Fialin and Chopin 2006), alkali-rich phases (e.g., Gedeon et al. 2008), and carbonates (e.g., Zhang et al. 2019). One extreme example concerns hydrated alkali-sulfate (natro-) jarosite and (natro-) alunite (K,Na)$(Al,Fe)_3(SO_4)_2(OH)_6$ displaying fine compositional variation at the scale of ~1–5 μm. Irremediable Na or K diffusion and a concomitant increase or decrease in Fe, Al, and S happen within <10 s of analyzing a single point at <2 nA with a slightly defocused beam (2–3 μm). Beyond this, the beam damage induces a large change in the major elements, and a TDI correction must be applied. In this case, it is possible to run analyses at 10 nA for 20 s using a focused electron beam and to correct for the beam damage effects. Beyond this point, the damage may become so severe that an accurate TDI correction cannot be applied. Notwithstanding a total electron dose of only 200 nA·s, and with the use of the TDI correction, the analytical precision is typically poor. Multiple point analyses in a homogeneous domain are then required to obtain a good precision, which can be problematic when the material to analyze is finely zoned at the micrometer-scale and in very small grains (typical grain-size in the sample under investigation is ~20 μm; Potter-McIntyre and McCollom 2018).
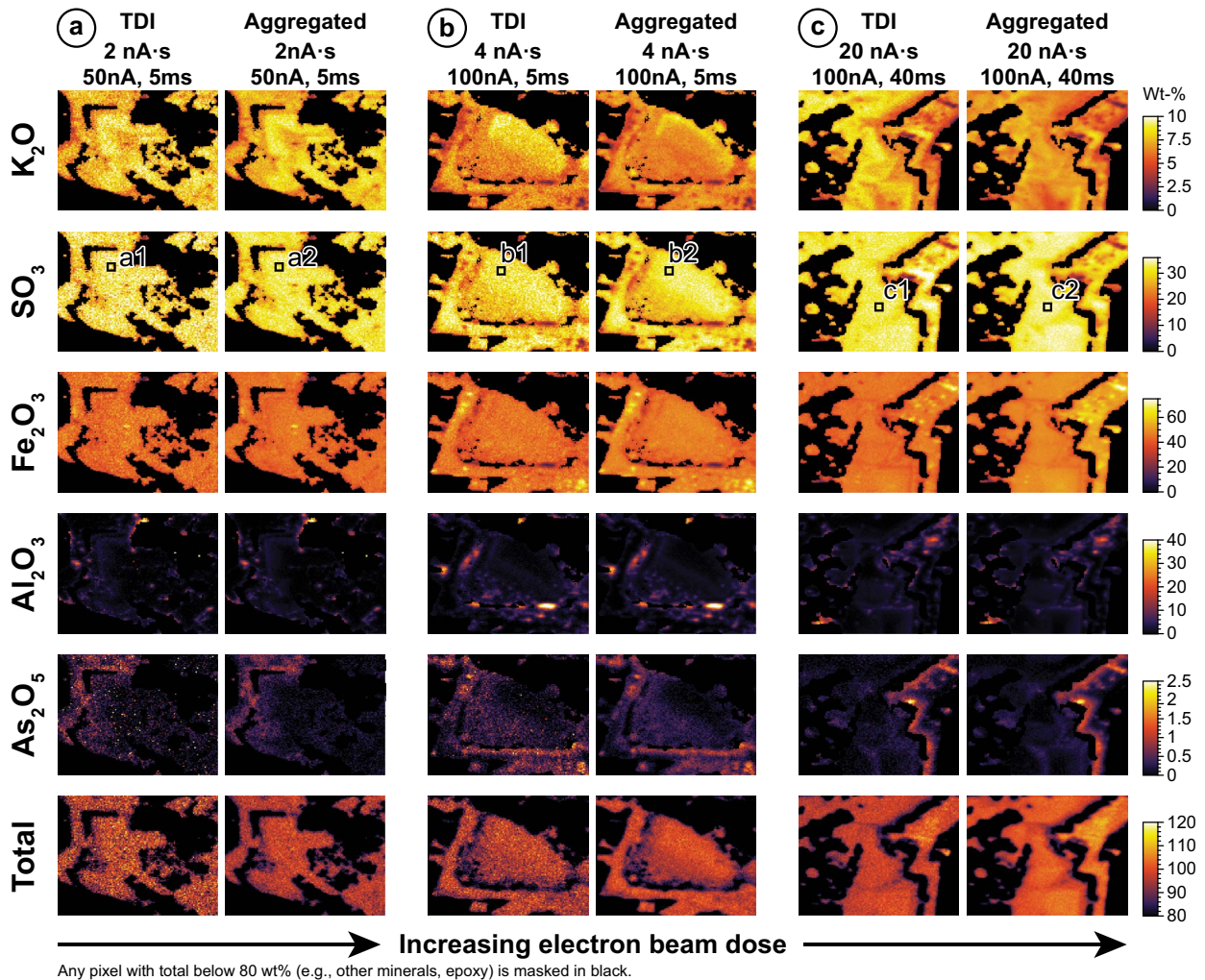
Another solution to obtain equally precise and sometimes better accuracy quantitative analyses of such complexly zoned beam sensitive materials is to acquire element maps and apply a TDI correction during the map quantification. To do this, a time series of beam (or stage) scanned maps over an area are acquired

with multiple (replicate) mapping frames. The TDI correction can then be applied on each individual pixel using these multiple frames to extrapolate the pixel intensity at time $t = 0$ s (beginning of the mapping elapsed time for each individual pixel). Figure 10 is an example of such TDI-corrected element maps of Na-free jarosite (see Potter-McIntyre and McCollom 2018 for detail on sample MN05, notably their Fig. 10). Multiple test maps for K$K\alpha$, S$K\alpha$, Fe$K\alpha$, Al$K\alpha$, and As$L\alpha$ are run using either 50 or 100 nA beam currents, different counting times (5, 10, 20, and 40 ms per pixel on one frame) and the total number of frames (eight frames at 5 ms, five frames for all others), resulting in a variation of total beam dose of 2 to 20 nA·s. Due to the beam damage induced by each test, it is not possible to reanalyze the same area. For the quantification of each map, the MAN background method is used, and the water content is recalculated by stoichiometry assuming six hydrogen atoms for a total of 14 O atoms and included in the iterated matrix correction routine (Fig. 2). Results obtained with and without the TDI correction are then compared, along with a comparison of data obtained on the first and the last frame (labeled, respectively "TDI," "Aggregated," "First," and "Last" in Fig. 10).

At low-beam dose (total of 2 nA·s per pixel; Fig. 10a), both the TDI-corrected maps and the aggregated maps yield identical results within their respective errors. It is clear from visual inspection and counting statistics that the TDI results are slightly less precise due to the nature of the TDI correction extrapolation. At intermediate to high-beam doses (e.g., 4 and 10 nA·s; Figs. 10b and 10c), the results of the aggregated maps degrade: zones are getting enriched or depleted in K_2O, and in parallel SO_3 and Fe_2O_3 either decrease or increase at high-beam dose, and overall the analytical totals increase. This can be clearly seen numerically in the averaged-pixel quantitative data (Fig. 10d), especially when comparing the data from the first and the last maps. It is also interesting to notice that there is no systematic diffusional loss of K, instead there are "sink and hole" areas where K diffuses in or out. This effect is illustrated in Figure 11 with a map of the TDI correction percentage for the measurement of K$K\alpha$, S$K\alpha$, and Fe$K\alpha$ over five passes at 100 nA and 40 ms per pixel (see also Fig. 10c).

Trace elements and spectrometer aggregation

Quantification of multiple phase X-ray maps can be easily done with great precision and accuracy for major and minor element analyses, but the counting statistics usually prohibits mapping for trace elements without excessively long acquisition times at high currents. If a high current is not applicable (e.g., beam sensitive materials) or if the analyst aims at reducing the total acquisition time, it is recommended to use multiple WDS detectors in parallel to analyze a single element. Figure 12 presents an X-ray map of a multiphase area in a rhyolite sample composed of glass, plagioclase, and K-feldspar. Previous single-point analyses and observations in BSE images suggest a strong Ba-enrichment at the rim of K-feldspar. Maps were acquired in two passes, with a first pass for the major elements (Si$K\alpha$, Al$K\alpha$, Ca$K\alpha$, Na$K\alpha$, and K$K\alpha$), and a second mapping pass with only Ba$L\alpha$ analysis on three PET-L spectrometers. Of the major elements expected in this sample, only Fe was not mapped, as it is a trace concentration in these specific feldspars and only pres-

Increasing electron beam dose

Any pixel with total below 80 wt% (e.g., other minerals, epoxy) is masked in black.

(d) 100-pixel averages (10x10 pixels; see location on SO₃ map)

	50 nA, 5 ms, 8 frames				100 nA, 5 ms, 8 frames				100 nA, 40 ms, 5 frames			
	a1 TDI	a2 Agg.	FIRST	LAST	b1 TDI	b2 Agg.	FIRST	LAST	c1 TDI	c2 Agg.	FIRST	LAST
K_2O	8.33(12)	8.24(8)	8.32	8.16	8.88(9)	7.16(4)	8.94	6.18	8.39(6)	7.12(3)	8.44	6.49
SO_3	33.0(5)	32.6(2)	33.2	32.0	32.5(3)	33.2(1)	32.4	34.0	32.91(14)	34.16(10)	32.8	34.9
Fe_2O_3	46.0(4)	45.5(2)	45.5	45.6	45.4(3)	47.8(2)	45.1	49.7	44.00(14)	48.08(8)	44.7	51.4
Al_2O_3	0.85(7)	0.79(5)	0.84	0.75	0.89(6)	0.87(4)	0.83	0.88	1.81(6)	1.92(5)	1.85	2.00
As_2O_5	0.18(6)	0.06(1)	0.08	0.05	0.05(1)	0.06(1)	0.06	0.08	0.12(1)	0.13(1)	0.10	0.13
H_2O*	11.48	11.46	11.48	11.55	11.07	11.03	11.04	10.98	11.57	11.39	11.55	11.25
Total	**99.30**	**98.10**	98.88	97.61	**98.70**	**100.13**	98.23	101.91	**98.28**	**102.43**	98.88	105.86

* Calculated by stoichiometry: 6 H for 14 O.

FIGURE 10. Quantified X-ray maps of jarosite in sample MN05 using a beam map at 15 keV with a focused beam. Field of view is 50 × 50 μm at ~0.39 μm/pixel resolution. Three separate examples are shown with increasing electron beam dose: (**a**) 50 nA, 5 ms dwell time, 8 frames (=2 nA·s), (**b**) 100 nA, 5 ms dwell time, 8 frames (=4 nA·s), and (**c**) 100 nA, 40 ms dwell time, 5 frames (=20 nA·s). For each test, the data was processed using either the TDI correction on each pixel, or by aggregating all intensities received on each frame (i.e., no correction for beam damage). All pixels yielding a low total below 80% were set to black. The table below lists the average of 100 pixels (area indicated on the SO₃ map) for the TDI corrected and aggregated data, respectively, along with the quantitative result considering only the first or the last acquired beam map frame. See text for discussion.
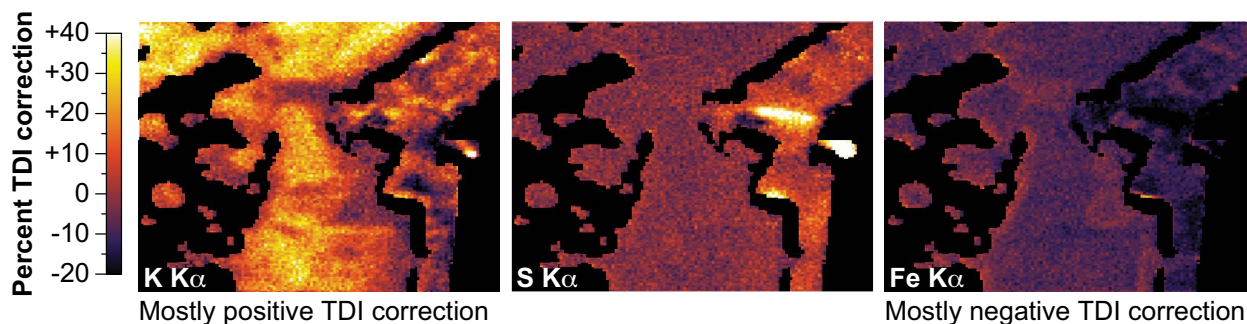
FIGURE 11. TDI correction (in relative percent) map for the analysis of K$K\alpha$, S$K\alpha$, and Fe$K\alpha$ at 100 nA, 40 ms per pixel, and with 5 passes (total beam dose is 20 nA·s).

▶**FIGURE 12.** Quantitative element mapping in rhyolite, with focus on Ba-content in plagioclase, K-feldspar, and glass. Conditions were 15 keV, 100 nA, and 40 ms per pixel, 2 passes. Field of view is 329.5 × 229.5 μm at 0.5 μm/pixel resolution. (**a**–**f**) Quantitative map of SiO_2, Al_2O_3, CaO, Na_2O, K_2O, and total wt%. (**g**) Quantitative BaO wt% map obtained by aggregating the intensity of three spectrometers equipped with L-type (large) PET monochromators. (**h**) Quantitative cross-section extracted from the map, as shown in **g**. Horizontal black lines over the BaO cross-section are precise data obtained from single-point quantitative analysis (longer counting time). (**i**) Quantitative single-point analysis shown for comparison; position of each analysis indicated in **g**.
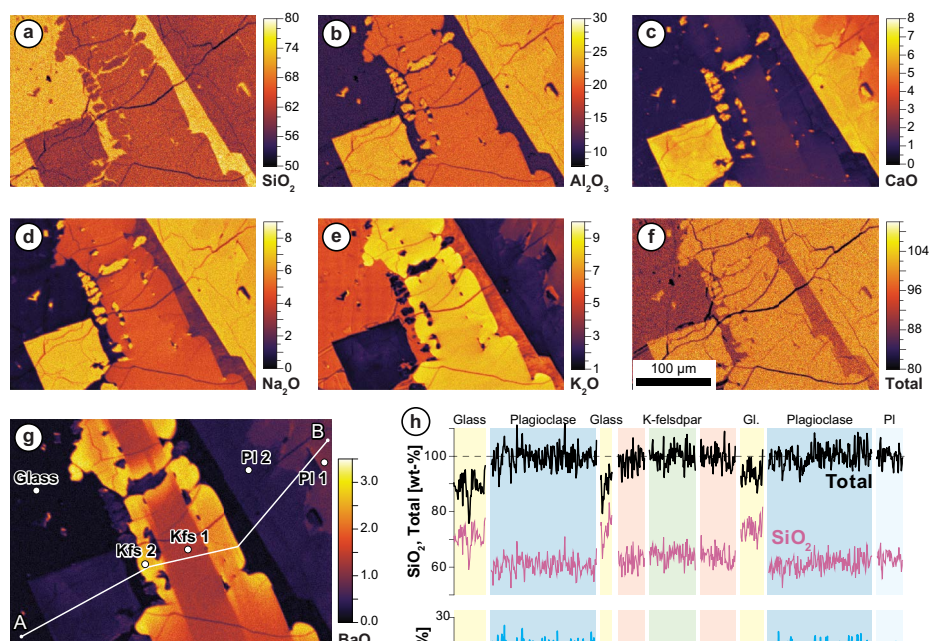
i Quantitative analysis point

	Kfs 1	Kfs 2	Pl 1	Pl 2	Glass
SiO_2	64.44	63.68	63.63	60.72	73.16
TiO_2	0.04	0.04	0.03	0.02	0.29
Al_2O_3	19.82	20.26	22.81	24.55	11.66
FeO	0.18	0.19	0.24	0.35	2.47
MnO	0.00	-0.01	0.00	0.00	0.05
MgO	0.01	0.01	0.01	0.01	0.05
CaO	1.42	0.89	3.71	6.12	0.78
SrO	0.09	0.08	0.11	0.09	0.01
BaO	1.28	2.75	0.83	0.32	0.12
Na_2O	4.80	4.31	6.22	6.67	2.17
K_2O	7.98	8.71	4.12	1.72	6.50
Total	100.06	100.91	101.72	100.59	97.26

ent at level around 2.5 wt% in the glass. All other elements (Mg, Ti, Sr, etc.) are below 1000 ppm. The presence of Ti could potentially be a problem for Ba analysis due to the mutual interference of Ti$K\alpha$ on Ba$L\alpha$. However, single-point analyses including a correction for this mutual Ti$K\alpha$ ↔ Ba$L\alpha$ interference yield low Ti-content: <3000 ppm in glass and <500 ppm in feldspar minerals. At this level, a correction for Ti interference on Ba is minimal and below the sensitivity of Ba$L\alpha$ element map (calculated Ba detection limit of ~500 ppm). These duplicate element maps allow one to not only highlight and quantify the high-Ba content in K-feldspar, but also to accurately and precisely analyze Ba even in the glass (~1200 ppm). These element maps were essential for the data interpretation, as only the maps clearly reveal a two-step growth. The primary feldspar, which is richer in albite (Na)-component, suffered a partial resorption (e.g., irregular internal zonation in Ca, Na, and K, top-right corner of Figs. 12c–e), and the Ba-rich K-feldspar rim and the

anorthite(Ca)-richer plagioclase rim both represent a second magmatic event.

IMPLICATIONS

Rigorous quantification of X-ray maps is critically important for accurate interpretation of element distributions, not only for minor and trace elements but also elements whose emission lines suffer significant absorption or fluorescence. Raw X-ray maps remain an essential tool to reveal two-dimensional variation that cannot be fully ascertained by discrete point analysis. However, because the same raw X-ray line intensity can represent quite different concentrations in different phases, due most notably to significant differences in X-ray absorption effect, but also from changes in background intensities (and potential issues stemming from spectral interferences), without quantification at the pixel level, it would be significantly riskier to draw robust conclusions from merely qualitative X-ray maps. Moreover, this rigorous quantification protocol ensures that all maps can be compared one-to-one, even if they were acquired at different times, using different spectrometers, in different laboratories, or at different analytical conditions, etc.

Applications of element map analysis by EPMA (WDS or EDS) are numerous, and the ability to quantify them with accuracy and precision makes these applications even more attractive to researchers. First, geological materials are often the product of a complex mineral growth, partial dissolution (resorption), and reprecipitation history, the interpretation of which is critical to developing an understanding of large-scale geological processes. Up until now, element maps were often only used for qualitative observations (e.g., identifying inherited core, retrogression, diffusion profile, etc., which subsequently required quantification by careful single-point analysis) or for approximate quantification (e.g., using a two-point calibration method in a single compositionally zoned phase). However, with the level of accuracy and precision achieved with the proposed map quantification methodology, the qualitative map data becomes quantitative data, with an accuracy comparable to a single point analysis and with equally good precision when pixel averaging is considered. Second, material scientists can now observe accurately and with high sensitivity diffusion profiles, identify and quantify exsolutions, or perform homogeneity tests. Additionally, the "analytical totals" map can also uncover previously unrecognized secondary fluorescence, i.e., pixels where the totals are consistently >100% (Fournelle et al. 2005). By extension, a more accurate "local" composition can be obtained in finely grained material (e.g., partially recrystallized glass or quenched material, exsolutions lamellae, etc.), without the need to acquire multiple discrete points on which the resulting accuracy can be questionable, due to the inhomogeneous nature of the analyzed material.

Finally, the complementary use of the mean atomic number background correction method allows one to apply an accurate background correction without the need to physically acquire additional background intensity maps with a resulting doubling (at least) of the total acquisition time. The use of spectral interference correction and time-dependent intensity correction routines also ensure that no such artifacts are present in the quantitative maps. As it follows the rigor and protocols of single-point analysis, this proposed mapping quantification method is most likely the best we can do, at present, in terms of accuracy for WDS X-ray map quantification. The acquisition of quantitative X-ray maps affords the analyst valuable quantitative data in less time when compared to a series of discrete point analysis in compositionally zoned materials or strongly heterogeneous materials or when the material is extremely beam sensitive.

REFERENCES CITED

Allaz, J.M., Williams, M., Jercinovic, M., Goemann, K., and Donovan, J. (2019a) Multipoint background analysis: Gaining precision and accuracy in microprobe trace element analysis. Microscopy and Microanalysis: The Official Journal of Microscopy Society of America, Microbeam Analysis Society, Microscopical Society of Canada, 25, 30–46.
Allaz, J.M., Popa, R.G., Reusser, E., and Martin, L. (2019b) Electron microprobe analysis of minor and trace elements in beam sensitive materials: How far can we go? Microscopy and Microanalysis, 25, 2312–2313.
Armstrong, J.T. (1988) Quantitative analysis of silicate and oxide materials: Comparison of Monte Carlo, ZAF, and procedures. Microbeam Analysis, 239–246.
Barkman, J., Carpenter, P., Zhao, J., and Donovan, J. (2013) Electron microprobe quantitative mapping vs. defocused beam analysis. Microscopy and Microanalysis, 19, 848–849.
Bastin, G.F., and Heijligers, H.J.M. (1991) Quantitative electron probe microanalysis of ultra-light elements (boron–oxygen). In K.F.J. Heinrich and D.E. Newbury, Eds., Electron Probe Quantitation, p. 145–161. Plenum Press.
Batanova, V.G., Sobolev, A.V., and Kuzmin, D.V. (2015) Trace element analysis of olivine: High precision analytical method for JEOL JXA-8230 electron probe microanalyser. Chemical Geology, 419, 149–157.
Borisova, A.Y., Zagrtdenov, N.R., Toplis, M.J., Donovan, J.J., Llovet, X., Asimow, P.D., de Parseval, P., and Gouy, G. (2018) Secondary fluorescence effects in microbeam analysis and their impacts on geospeedometry and geothermometry. Chemical Geology, 490, 22–29.
Carpenter, P.K., and Hahn, T. (2017) New developments in compositional stage mapping by epma and micro-XRF. Microscopy and Microanalysis, 23, 1068–1069.
Chantler, C.T. (2000) Detailed Tabulation of atomic form factors, photoelectric absorption and scattering cross section, and mass attenuation coefficients in the vicinity of absorption edges in the soft X-ray (Z=30–36, Z=60–89, E=0.1 keV–10 keV), addressing convergence issues of earlier work. Journal of Physical and Chemical Reference Data, 29, 597–1048.
Chantler, C.T., Olsen, K., Dragoset, R.A., Chang, J., Kishore, A.R., Kotochigova, S.A., and Zucker, D.S. (2005) X-ray form factor, attenuation and scattering tables (version 2.1) (online). Available: http://physics.nist.gov/ffast (accessed: July 29, 2020). National Institute of Standards and Technology, Gaithersburg, Maryland.
Donovan, J.J., and Tingle, T.N. (1996) An improved mean atomic number correction for quantitative microanalysis. Microscopy and Microanalysis, 2, 1–7.
Donovan, J.J., Snyder, D.A., and Rivers, M.L. (1993) An improved interference correction for trace element analysis. Microbeam Analysis, 2, 23–28.
Donovan, J.J., Lowers, H.A., and Rusk, B.G. (2011) Improved electron probe microanalysis of trace elements in quartz. American Mineralogist, 96, 274–282.
Donovan, J.J., Singer, J.W., and Armstrong, J.T. (2016) A new EPMA method for fast trace element analysis in simple matrices. American Mineralogist, 101, 1839–1853.
Donovan, J., Pinard, P., and Demers, H. (2019) High speed matrix corrections for quantitative X-ray microanalysis based on Monte Carlo simulated K-ratio

intensities. Microscopy and Microanalysis : The Official Journal of Microscopy Society of America, Microbeam Analysis Society, Microscopical Society of Canada, 25, 735–742.

Eichen, E., Tabock, J., and Kinsman, K.R. (1972) An electron-microprobe technique for detecting low carbon concentrations in iron. Metallography, 5, 151–162.

Fialin, M., and Chopin, C. (2006) Electron-beam (5–10 keV) damage in triplite-group phosphates: Consequences for electron-microprobe analysis of fluorine. American Mineralogist, 91, 503–510.

Fiedrich, A.M., Bachmann, O., Ulmer, P., Deering, C.D., Kunze, K., and Leuthold, J. (2017) Mineralogical, geochemical, and textural indicators of crystal accumulation in the Adamello Batholith (Northern Italy). American Mineralogist, 102, 2467–2483.

Fournelle, J.H., Kim, S., and Perepezko, J.H. (2005) Monte Carlo simulation of Nb Kα secondary fluorescence in EPMA: Comparison of PENELOPE simulations with experimental results. Surface and Interface Analysis, 37, 1012–1016.

Gedeon, O., Zemek, J., and Jurek, K. (2008) Changes in alkali-silicate glasses induced with electron irradiation. Journal of Non-Crystalline Solids, 354, 1169–1171.

Goldoff, B., Webster, J.D., and Harlov, D.E. (2012) Characterization of fluor-chlorapatites by electron probe microanalysis with a focus on time-dependent intensity variation of halogens. American Mineralogist, 97, 1103–1115.

Goldstein, J.I., Newbury, D.E., Echlin, P., Joy, D.C., Firori, C., and Lifshin, E. (1992) Scanning Electron Microscopy and X-ray Microanalysis, 550 p. Springer-Verlag.

Hughes, E.C., Buse, B., Kearns, S.L., Blundy, J.D., Kilgour, G., and Mader, H.M. (2019) Low analytical totals in EPMA of hydrous silicate glass due to sub-surface charging: Obtaining accurate volatiles by difference. Chemical Geology, 505, 48–56.

Jercinovic, M.J., Williams, M.L., Allaz, J., and Donovan, J.J. (2012) Trace analysis in EPMA. IOP Conference Series: Materials Science and Engineering, 32, 012012.

Kramers, H.A. (1923) On the theory of X-ray absorption and of the continuous X-ray spectrum. The London, Edinburgh, and Dublin Philosophical Magazine and Journal of Science, 46, 836–871.

Lanari, P., Vidal, O., De Andrade, V., Dubacq, B., Lewin, E., Grosch, E.G., and Schwartz, S. (2014) XMapTools: A MATLAB©-based program for electron microprobe X-ray image processing and geothermobarometry. Computers & Geosciences, 62, 227–240.

Merlet, C., and Bodinier, J.-L. (1990) Electron microprobe determination of minor and trace transition elements in silicate minerals: A method and its application to mineral zoning in the peridotite nodule PHN 1611. Chemical

Geology, 83, 55–69.

Morgan, G.B., and London, D. (1996) Optimizing the electron microprobe analysis of hydrous alkali aluminosilicate glasses. American Mineralogist, 81, 1176–1185.

Moy, A., Fournelle, J.H., and Von Der Handt, A. (2019) Solving the iron quantification problem in low-kV EPMA: An essential step toward improved analytical spatial resolution in electron probe microanalysis—Olivines. American Mineralogist, 104, 1131–1142.

Newbury, D.E. (1995) Artifacts in energy dispersive X-ray spectrometry in electron beam instruments. are things getting any better? In D.B. Williams, J.I. Goldstein, and D.E. Newbury, Eds., X-ray Spectrometry in Electron Beam Instruments, p. 167–201. Springer.

Newbury, D., and Ritchie, N. (2019) Electron-excited X-ray microanalysis by energy dispersive spectrometry at 50: Analytical accuracy, precision, trace sensitivity, and quantitative compositional mapping. Microscopy and Micro-analysis, 25, 1075–1105.

Nielsen, C.H., and Sigurdsson, H. (1981) Quantitative methods for electron microprobe analysis of sodium in natural and synthetic glasses. American Mineralogist, 66, 547–552.

Ortolano, G., Visalli, R., Godard, G., and Cirrincione, R. (2018) Quantitative X-ray Map Analyser (Q-XRMA): a new GIS-based statistical approach to mineral image analysis. Computers & Geosciences, 115, 56–65.

Potter-McIntyre, S.L., and McCollom, T.M. (2018) Jarosite and alunite in ancient terrestrial sedimentary rocks: Reinterpreting Martian depositional and diagenetic environmental conditions. Life, 8, 32.

Robaut, F., Crisci, A., Durand-Charre, M., and Jouanne, D. (2006) Practical aspects of carbon content determination in carburized steels by EPMA. Microscopy and Microanalysis: The Official Journal of Microscopy Society of America, Microbeam Analysis Society, Microscopical Society of Canada, 12, 331–334.

Tinkham, D.K., and Ghent, E.D. (2005) XRMapAnal: A program for analysis of quantitative X-ray maps. American Mineralogist, 90, 737–744.

Zhang, X., Yang, S., Zhao, H., Jiang, S., Zhang, R., and Xie, J. (2019) Effect of beam current and diameter on electron probe microanalysis of carbonate minerals. Journal of Earth Science, 30, 834–842.